

# Simulating the 21-cm signal from reionisation including non-linear ionisations and inhomogeneous recombinations

Sultan Hassan<sup>1</sup>, Romeel Davé<sup>1,2,3</sup>, Kristian Finlator<sup>4,5</sup>, Mario G. Santos<sup>1,6,7</sup>

<sup>1</sup> *University of the Western Cape, Bellville, Cape Town, 7535, South Africa*

<sup>2</sup> *South African Astronomical Observatories, Observatory, Cape Town, 7925, South Africa*

<sup>3</sup> *African Institute for Mathematical Sciences, Muizenberg, Cape Town, 7945, South Africa*

<sup>4</sup> *Dark Institute of Cosmology, Niels Bohr Institute, University of Copenhagen, Copenhagen, 2100, Denmark*

<sup>5</sup> *New Mexico State University, Las Cruces, NM 88003, United States*

<sup>6</sup> *SKA SA, The Park, Park Road, Pinelands 7405, South Africa*

<sup>7</sup> *CENTRA, Instituto Superior Técnico, Universidade de Lisboa, Lisboa 1049-001, Portugal*

15 October 2018

## ABSTRACT

We explore the impact of incorporating physically motivated ionisation and recombination rates on the history and topology of cosmic reionisation and the resulting 21-cm power spectrum, by incorporating inputs from small-volume hydrodynamic simulations into our semi-numerical code, SIMFAST21, that evolves reionisation on large scales. We employ radiative hydrodynamic simulations to parameterize the ionisation rate  $R_{\text{ion}}$  and recombination rate  $R_{\text{rec}}$  as functions of halo mass, overdensity and redshift. We find that  $R_{\text{ion}}$  scales super-linearly with halo mass ( $R_{\text{ion}} \propto M_h^{1.41}$ ), in contrast to previous assumptions. Implementing these scalings into SIMFAST21, we tune our one free parameter, the escape fraction  $f_{\text{esc}}$ , to simultaneously reproduce recent observations of the Thomson optical depth, ionizing emissivity, and volume-averaged neutral fraction by the end of reionisation. This yields  $f_{\text{esc}} = 4_{-2}^{+7}\%$  averaged over our  $0.375h^{-1}\text{Mpc}$  cells, independent of halo mass or redshift, increasing to 6% if we also constrain to match the observed  $z = 7$  star formation rate function. Introducing super-linear  $R_{\text{ion}}$  increases the duration of reionisation and boosts small-scale 21-cm power by  $\times 2 - 3$  at intermediate phases of reionisation, while inhomogeneous recombinations reduce ionised bubble sizes and suppress large-scale 21-cm power by  $\times 2 - 3$ . Gas clumping on sub-cell scales has a minimal effect on the 21cm power. Super-linear  $R_{\text{ion}}$  also significantly increases the median halo mass scale for ionising photon output to  $\sim 10^{10}M_{\odot}$ , making the majority of reionising sources more accessible to next-generation facilities. These results highlight the importance of accurately treating ionising sources and recombinations for modeling reionisation and its 21-cm power spectrum.

**Key words:** galaxies: evolution - galaxies: formation - galaxies: high-redshift - cosmology: theory - dark ages, reionization, first stars early Universe.

## 1 INTRODUCTION

The epoch of reionisation (EoR) is the last global phase transition of the Universe, during which the birth of first luminous sources gradually ionised the intergalactic medium (IGM). Given that this epoch remains mostly unexplored, current EoR studies are devoted to answering its most basic questions: When did the EoR begin? What are the sources responsible for driving reionisation? How did the topology of reionisation evolve? When did the EoR end? Accurate answers for these questions are crucial to understand the early stages of galaxy formation and evolution.

Observations of the high-redshift quasars' Ly $\alpha$  absorption spectra (Becker et al 2001; Fan et al 2006) suggest that reionisation of the IGM completed about  $z \sim 6$ , though there is some evidence for variations in this (Pentericci et al. 2014; Becker & Bolton et al 2015; Chardin et al. 2015). The recent cosmic microwave background (CMB) polarization measurements by Planck (2015) reported a Thomson electron scattering optical depth out to the surface of last scattering of 0.066, lower than previous measures by WMAP (Hinshaw et al. 2013), thus reducing the need for exotic ionising sources within high redshift star-forming galaxies (Robertson et al

2015). These observations constrain the topology, sources, and evolution of the EoR, albeit only crudely. The detailed evolution of spatially-inhomogeneous reionisation involves a complex interplay between evolving source populations, the propagation of ionising photons within a patchy IGM, and the enrichment of the first galaxies and halos that may affect the nature of the ionising sources.

A promising approach to tracking the evolution of neutral hydrogen during the EoR is via its emission in the redshifted hyperfine 21-cm line. The advantage of using the 21-cm line is that its brightness temperature is directly proportional to neutral gas content ( $x_{\text{HI}}$ ) which makes it possible to study the three-dimensional distribution of the neutral gas and the large scale structure during the EoR (Barkana & Loeb 2001; Furlanetto et al 2006). Hence the EoR is a key science goal for current and future low-frequency ( $\sim 150$  MHz) radio telescopes. These experiments include the Low Frequency Array (LOFAR)<sup>1</sup>, the Murchison Wide-field Array (MWA)<sup>2</sup>, the Precision Array to Probe Epoch of Reionisation (PAPER)<sup>3</sup>, the Hydrogen Epoch of Reionisation Array (HERA)<sup>4</sup> and eventually the Square Kilometer Array (SKA-Low)<sup>5</sup>. Owing to the relatively coarse angular resolution at these long wavelengths, interpreting these observations fully requires understanding how small-scale processes such as the production and propagation of ionising photons impact the large-scale neutral gas distribution.

To this end, numerous theoretical studies have focused on modeling the EoR process and its expected 21-cm signal. A key limiting factor is the need for vast dynamic range that remains a computational challenge. Proper cosmological simulations of the EoR must resolve the smallest proto-galaxies to track the local generation and propagation of the ionizing photons, as well as their recombinations which requires modeling the small-scale clumping of gas, from sub-kpc scales up to the sizes of the largest ionising bubbles during the late stages of the EoR, believed to be tens of Mpc (e.g. Sobacchi & Mesinger 2014). This requires both large-volume simulations together with extremely high resolution. For instance, the forthcoming EoR surveys by SKA-Low will span a field-of-view of about 10 degrees that corresponds to a size of  $\sim 500$  Mpc with  $\sim 0.5$  Mpc resolution (Iliev et al. 2015), while the proto-galaxies that are thought to provide the dominant source of ionising photons likely have scale sizes below a kpc (e.g. Tilvi et al. 2013).

Early hydrodynamic simulations of the EoR applied post-processed radiative transfer to cosmologically-evolved density fields (e.g. Gnedin 2000; Razoumov et al 2002; Mellema et al 2006; McQuinn et al 2007; Thomas et al 2009; Iliev et al. 2014; Bauer et al. 2015), which enabled the study of reionisation topology but did not self-consistently include the feedback effects of the ionisation on galaxies. More recent codes such as MARCH (Finlator & Davé 2009; Finlator et al. 2013) and TRAPHIC (Pawlik & Schaye 2008) have been developed to do full radiative hydrodynamics in a cosmological galaxy formation code, including feedback

processes constrained to match available high- $z$  data (Finlator et al. 2011). Unfortunately, these simulations are computationally very expensive, and the requirement that the simulation resolve to below the hydrogen cooling halo mass limit of  $\sim 10^8 M_{\odot}$  drives one to a quite small box size (see however So et al 2014; Gnedin & Kaurov 2014), typically  $\lesssim 10$  Mpc.

A complementary approach is to use a large volume ( $\gtrsim 100$  Mpc) simulations that employ physically-motivated parameterizations to determine the location and evolution of the source population, even though they do not resolve individual galaxy sources. These so-called semi-numerical models have low computational cost since they do not require radiative transfer and they determine the density field evolution from analytic prescriptions such as excursion set formalism (Mesinger & Furlanetto 2007; Zahn et al 2007; Choudhury et al 2009; Santos et al. 2010). A key free parameter in such codes is the ionizing efficiency per unit (halo) mass, generally assumed to be constant and tuned to match key observations. Semi-numerical models have been shown to roughly reproduce the ionisation history and 21-cm power spectrum as obtained from radiative hydrodynamic simulations (Zahn et al 2011; Majumdar et al 2014). However, the simplicity of the source parameterisations and the fact that they neglect recombinations means that they fail to account for all of the relevant inhomogeneous physical processes required to properly address the problem.

Sobacchi & Mesinger (2014) have recently improved their semi-numerical code by incorporating inhomogeneous recombinations using a sub-grid prescription that self-consistently tracks the evolution of ionizing sources and recombination systems, as well as accounting for feedback effects. While an improvement over previous semi-numerical work, the parameterisations are obtained without self-consistently accounting for galactic feedback processes, and hence still employ a constant efficiency parameter (i.e. ionising photon rate per unit dark matter halo mass  $M_h$ ) to characterise the source population. In contrast, radiative hydrodynamic simulations tuned to match high- $z$  galaxy properties find that the star formation rate, and hence relatedly the ionising photon rate, scales super-linearly with halo mass at these epochs, typically as  $M_h^{1.3-1.4}$  (Finlator et al. 2011). Furthermore, the clumping factor that controls the recombination rate is set by a complex interplay between photon propagation as a function of environment, which is best followed using full radiative hydrodynamic simulations (e.g. Finlator et al. 2012). Hence there remains room for improvement in semi-numerical EoR models.

In this paper we aim to take the next step by implementing calibrated relations for the non-linearly mass-dependent ionisation efficiency and inhomogeneous recombination rates taken from high-resolution radiative hydrodynamic (RT) simulations into the semi-numerical EoR code SIMFAST21 (Santos et al. 2010). We use simulations from Finlator et al. (2015) that have been previously calibrated to match various observations of galaxies at high redshifts. We derive new parametrizations for the non-linear ionisation ( $R_{\text{ion}}$ ) and recombination ( $R_{\text{rec}}$ ) rates directly from this radiative hydrodynamic simulation as a function of halo mass and redshift, complemented by a larger-volume galaxy formation simulation without radiative transfer to help bridge the small scales in the RT simulation to the large-scale semi-

<sup>1</sup> <http://www.lofar.org/>

<sup>2</sup> <http://www.haystack.mit.edu/ast/arrays/mwa/>

<sup>3</sup> <http://w.astro.berkeley.edu/~dbacker/eor/>

<sup>4</sup> <http://reionisation.org>

<sup>5</sup> <https://www.skatelescope.org>

numerical model. We implement these new formulae for  $R_{\text{ion}}$  and  $R_{\text{rec}}$  that track the evolution of the non-linear ionisations and inhomogeneous recombinations into SIMFAST21. We constrain our one free model parameter, the escape fraction, to simultaneously match observations of the Planck Thomson optical depth, the late evolution of the Lyman alpha mean opacity, and the ionising emissivity at  $z \sim 5$ . Finally, we make predictions for the expected 21-cm power spectrum from the EoR, and particularly investigate how our new physical parameterisations alter the predicted signal. This new version of our SIMFAST21 will soon be publicly available<sup>6</sup>.

This paper is organized as follows: In section 2, we introduce the simulations used, namely SIMFAST21, the radiative hydrodynamic simulations, and the non-radiative larger-volume simulation. In section 3, we present our new parametrizations of  $R_{\text{rec}}$  and  $R_{\text{ion}}$  from hydrodynamic simulations. We present our key observables in section 4, explore the impact of our new parameterisations in section 5 and conclude in section 6. Throughout this work, we adopt a  $\Lambda$ CDM cosmology in which  $\Omega_M = 0.3$ ,  $\Omega_\Lambda = 0.7$ ,  $h \equiv H_0/(100 \text{ km/s/Mpc}) = 0.7$ , a primordial power spectrum index  $n = 0.96$ , an amplitude of the mass fluctuations scaled to  $\sigma_8 = 0.8$ , and  $\Omega_b = 0.045$ . We quote all results in comoving units, unless otherwise stated.

## 2 SIMULATIONS

We describe SIMFAST21 (Santos et al. 2010) and, in particular, focus on how the ionized regions are identified using a fixed efficiency parameter. We then briefly describe the two complementary suites of the state-of-the-art hydrodynamic simulations, namely a high-resolution radiative hydrodynamic simulation (**6/256-RT**; Finlator et al. 2015), and a larger-volume cosmological hydrodynamic simulation without radiative transfer (**32/512**; Davé et al. 2013), which we employ to obtain new parametrizations of the non-linear ionisation and inhomogeneous recombination rates. A summary of our simulations is shown below in Table 1.

### 2.1 SIMFAST21

SIMFAST21 is a semi-numerical code that predicts the redshifted 21-cm signal from cosmic reionisation. SIMFAST21 simulation uses a Monte-Carlo approach to evolve the density field from a Gaussian random initial state to form collapsed structures based on a spherical collapse density threshold. This prescription generally follows the algorithm described in Mesinger & Furlanetto (2007), which we briefly review here.

At very high redshift, the dark matter density field is distributed linearly onto a grid, and the linear gravitational corrections are added by applying the Zel'Dovich (1970) approximation to evolve to lower redshifts. The collapsed dark matter halos are specified using the excursion-set formalism with an overdensity threshold of  $\delta_c(z) \sim 1.68/D(z)$ , where  $D(z)$  is the linear growth factor.

Ionized regions are identified using a similar form of

the excursion-set algorithm, based on the assumption of a constant efficiency parameter of ionising photon per unit halo mass,  $\zeta$ . The ionisation condition for any given region is simply the amount of collapsed dark matter halo  $f_{\text{coll}}$  compared with the efficiency parameter  $\zeta$ . In other words, the region is considered to be fully ionized if:

$$f_{\text{coll}} \geq \zeta^{-1}, \quad (1)$$

and fully neutral if not. For single cells which are not covered by ionised bubbles, we set their ionised fraction to  $f_{\text{coll}}\zeta$ . Using this condition, the ionisation field is generated that is the main input required to compute the predicted 21-cm signal.  $\zeta$  encapsulates a mixture of the ionisation and recombination processes such as ionising radiation escape fraction and recombinations by Lyman Limit Systems (LLS). However, it implicitly assumes that the recombinations trace the halos in the same way as the ionisations, which is unlikely to be true in detail. Nonetheless,  $\zeta$  can be tuned to match observations and yield predicted 21-cm power spectra.

In §3.3 we will describe our improvements to this scheme. In particular, we aim to improve the following aspects from the previous version of SIMFAST21:

- No explicit modeling of recombinations. Recombinations are only implicitly modeled via the constant efficiency parameter, which does not account for inhomogeneities in the density field and the local clumping factor.
- The use of a constant efficiency parameter. We will show that this is not an optimal description of the ionisation rate as a function of halo mass.
- Regions identified as fully ionised are set to have a neutral fraction of zero. More realistically, they should have a small neutral fraction appropriate for an optically-thin portion of the Universe in ionisation equilibrium.
- The density field spatial distribution. The original code uses nearest grid point assignment of density field to cells, but this can result in a biased density field distribution with unexpected voids when applying the Zel'Dovich (1970) approximation.

A typical run with SIMFAST21 will have a volume of several hundred Mpc and a cell size of several hundred kpc. Hence this method cannot resolve the galaxies that are the sources of ionising photons in the EoR, nor the clumped density field that governs recombinations. Therefore, to develop a better sub-grid model for these processes, we need to employ high-resolution hydrodynamic simulations of galaxy formation that can resolve these processes directly. Next we describe these hydrodynamic simulations.

### 2.2 6/256-RT simulation

To resolve the smallest significantly star-forming halos, we use the recent radiative transfer cosmological hydrodynamic simulation described more fully in Finlator et al. (2015). This simulation uses the GADGET-3 Smoothed Particle Hydrodynamics (SPH) code (Springel 2005), merged with the radiative transfer code MARCH (Finlator & Davé 2009; Finlator et al. 2012) to run a fully self-consistent radiative hydrodynamic simulation of early galaxy formation. Built on the version of GADGET developed by Oppenheimer & Davé (2008), this code incorporates well-constrained models for

<sup>6</sup> <https://github.com/mariogrs/Simfast21>

star formation-driven feedback processes, that do a generally good job of matching observed lower-redshift galaxy and IGM properties (Oppenheimer & Davé 2008; Davé, Oppenheimer, & Finlator 2011; Davé, Finlator, & Oppenheimer 2011; Davé et al. 2013).

The particular run we use, which we will call **6/256-RT**, employs a small volume of  $6h^{-1}\text{Mpc}$  and evolves  $2 \times 256^3$  particles. The mass of each gas particle is  $2.3 \times 10^5 M_\odot$  whereas the dark matter particle is about  $5.6 \times$  more massive. We therefore can resolve halos down to hydrogen cooling limit at  $10^8 M_\odot$  with 65 (dark matter+gas) particles, and galaxies down to stellar masses of  $7.4 \times 10^6 M_\odot$  with 32 gas particles. The equivalent Plummer gravitational softening length employed is 469 pc (comoving), corresponding to around 50 physical pc at the epoch of interest. It is crucial that our simulation resolves halos down to the hydrogen cooling limit, and therefore should be resolving essentially all the ionising photon output during the EoR under the assumption that halos below the hydrogen cooling limit do not contribute substantially to the photon budget, as is now generally believed (e.g. Wise & Cen 2009).

This simulation also includes a subgrid Monte Carlo model for kinetic galactic outflows, following the “ezw” prescription described in Davé et al. (2013). The two free parameters are the mass loading factor  $\eta$  and wind speed  $v_w$ , which vary with galaxy velocity dispersion  $\sigma$  that is calculated using an on-the-fly friends-of-friends galaxy identification code. The ezw prescription employs momentum-driven wind scalings ( $v_w \propto \sigma$  and  $\eta \propto \sigma^{-1}$ ) in sizable galaxies ( $\sigma > 75 \text{ km s}^{-1}$ ), and energy driven scalings ( $\eta \propto \sigma^{-2}$ ) in dwarf galaxies. To mock up outflows blowing channels through the interstellar medium (ISM), hydrodynamic forces are turned off until either the particle reaches 10% of SF critical density or a time of  $1.95 \times 10^{10}/(v_w(\text{km s}^{-1}))$  yr has passed. These scalings result in many predictions for galaxy and IGM properties that agree reasonably well with observations (Somerville et al. 2015). This version of GADGET also includes a model for chemical enrichment following Type II and Type Ia supernovae and stellar evolution, as well as primordial and metal cooling. The star formation model follows the multi-phase model in Springel & Hernquist (2003b), with a density threshold of  $n_{\text{H}} = 0.13 \text{ cm}^{-3}$ . A Chabrier (2003) initial mass function (IMF) is assumed throughout. Radiative cooling follows the prescription in Katz et al. (1996) to include the primordial cooling, and Sutherland & Dopita (1993) collisional ionisation equilibrium tables to account for cooling from metal lines.

The radiative transfer is done during the simulation run on a grid of  $32^3$  voxels, and its evolution is tracked using a moment-based method, together with a long characteristics code periodically employed to calculate the Eddington tensor in each cell in order to close the moment hierarchy (Finlator et al. 2011). The non-equilibrium ionisation state of the gas is followed by interpolating the ionisation field to the location of each gas particle. Sixteen separate frequency groups are followed, evenly spaced between 1 – 10 Ryd.

While the code is high resolution by cosmological standards, it lacks sufficient resolution to directly predict the escape of ionising photons from star-forming regions. Hence there is still an assumption required for the escape fraction of ionising photons,  $f_{\text{esc}}$ . In this run, a mass- and redshift-dependent  $f_{\text{esc}}$  is employed, which results in  $f_{\text{esc}} = 0.8$  in

halos with mass  $M_{\text{h}} < 10^8 M_\odot$ , dropping with both mass and time to around 5% at  $z = 5$  in more massive halos; the full formula is in equation 1 of Finlator et al. (2015).

Finlator et al. (2015) showed that this simulation, with its  $f_{\text{esc}}$  as assumed, can simultaneously match two key EoR observations, namely the optical depth to Thomson scattering from the Wilkinson Microwave Anisotropy Probe (WMAP; Hinshaw et al. 2013) polarization-temperature cross-correlation, and the volume-averaged neutral fraction at  $z \sim 6$  (Fan et al. 2006) measured from the Ly $\alpha$  forest. Hence it is a plausible model for the evolution of the ionising background during the EoR.

As an important aside, we point out an inconsistency in this paper regarding our assumed  $f_{\text{esc}}$ : We will use this RT simulation’s output to provide a description for the ionising photon rate that we will implement into SIMFAST21, but then we will re-tune  $f_{\text{esc}}$  in our semi-numerical runs to a substantially different value than what was assumed in the RT simulation. Ideally, we would re-run our RT simulation with the new  $f_{\text{esc}}$ , and iterate until convergence. Beyond the prohibitive computational cost to do so, there is a more fundamental reason why this is not feasible: The volume of our RT simulation is too small to fully capture even the moderately massive halos that (as we show later) contribute significantly to the ionising photon budget particularly during the latter stages of the EoR. Therefore, the  $f_{\text{esc}}$  used in the RT simulation is tuned to high values at early stages of the EoR to compensate for those missing halos. However, the critical input from RT simulation is the slope of the star formation rate – halo mass (SFR– $M_{\text{h}}$ ) relation (SFR  $M_{\text{h}}^{1.3-1.4}$ ), which is sensitive to feedback from stellar energy and the UVB at low masses. Hence it is appropriate to boost the  $f_{\text{esc}}$  in the RT simulation in order to model a realistic UVB evolution, as this in turn yields a more realistic SFR( $M_{\text{h}}, z$ ) prediction. Although the  $f_{\text{esc}}$  assumed in the RT simulation is not self-consistent, the fact that it reproduces key EoR observables including the UV luminosity function means that it likely represents a plausible evolution for the ionising photon output and neutral gas density field over the scales that are modeled. Hence while at present there is no practical way to avoid this inconsistency, it nonetheless provides an appropriate characterisation of the parameters we need for our large-scale modeling.

### 2.3 32/512 simulation

While the RT simulation described above accurately follows the interplay between photoionisation and galaxy formation, it lacks the volume to produce sufficiently large halos that are an important contributor to reionisation. Since we want to evolve large volumes with SIMFAST21, we would like to have an “intermediate” sized simulation that effectively bridges the gap, and allows the computation of ionisation and recombination rates in more massive halos. For this purpose, we will use a larger-volume cosmological hydrodynamic simulation that does not include radiative transfer. As discussed in Finlator et al. (2012), radiative transfer effects are only important in “photo-sensitive” halos with  $M_{\text{h}} \lesssim 10^{9.3} M_\odot$ , and hence we will only utilize this simulation for halos larger than this.

The simulation we employ has been fully described in Davé et al. (2013); here we review the basic details. This

simulation uses the GADGET-2 N-body+SPH code (Springel 2005) to model a cubic volume of  $32h^{-1}\text{Mpc}$  on a side and  $512^3$  particles of dark matter and gas each; we refer to this as our **32/512** run. Each gas particle has a mass of about  $4.5 \times 10^6 M_\odot$ , allowing us to resolve galaxies down to stellar masses of around  $M_{*,\text{lim}} = 1.4 \times 10^8 M_\odot$ , and halo masses of around  $10^9 M_\odot$ .

Most of the physics is identical to the RT run, including the radiative cooling, star formation following Springel & Hernquist (2003), the chemical evolution model, and the “ezw” prescription for galactic outflows. One difference is that, unlike in the RT run, ionisation equilibrium is assumed throughout, taking a spatially-uniform ionising background as given by Haardt & Madau (2001). Also, this simulation includes a model to quench star formation in massive galaxies, but this does not come into play at the early epochs that we consider here.

The overall strategy is to parameterise the ionisation and recombination rates taken from the **6/256-RT** and **32/512** runs, and insert those parameterisations into SIMFAST21. Next we describe how this is done.

### 3 PARAMETERIZING IONISATIONS AND RECOMBINATIONS

We aim to obtain new parameterizations of  $R_{\text{ion}}$  and  $R_{\text{rec}}$  that capture environmental and feedback effects directly from the **32/512** and **6/256-RT** simulations, in order to implement them into SIMFAST21. To begin, we must determine the ionisation and recombination rates of our simulated gas particles.

#### 3.1 Ionisation Rate, $R_{\text{ion}}$

To determine the ionisation rate of each gas particle, we take directly from the **6/256-RT** and **32/512** simulations output the star formation rate (SFR) and metallicity ( $Z$ ). We then compute the ionisation rate using Equation (2) in Finlator et al. (2011), which is derived from Schaerer (2003) models. Given an ionisation photon output rate for each particle, we then sum this over all the star-forming gas particles within a given halo to determine  $R_{\text{ion}}$  for that halo.

In Figure 1, we show  $R_{\text{ion}}$  as a function of halo mass for halos at  $z = 6, 7, 8$  (top to bottom panels). To increase dynamic range, we combine the **6/256-RT** (green dots) and **32/512** (blue dots) simulations, thereby covering dark matter halo masses of  $M_h \sim 10^{8-11.5} M_\odot$ . Importantly, the values of  $R_{\text{ion}}$  among the two simulations is quite similar in the overlap region of  $M_h \sim 10^{9.3-10} M_\odot$ , with only a very slight tendency for the smaller volume to have higher  $R_{\text{ion}}$ . At low halo masses ( $M_h \lesssim 10^8 M_\odot$ ) we see a turn-down in  $R_{\text{ion}}$  owing to photo-suppression of galaxy formation (Finlator et al. 2011). At high masses,  $R_{\text{ion}}$  follows a power law that is approximately  $R_{\text{ion}} \propto M_h^{1.4}$ , consistent with what the dependence on SFR with  $M_h$  found in similar simulations by Finlator et al. (2011).

The red vertical error bars show the  $1\sigma$  scatter in  $R_{\text{ion}}$  in  $\log M_h$  bins of 0.5. At  $M_h = 10^{10} M_\odot$ ,  $\sigma \sim 0.12$  independent of redshift. Note that when implementing  $R_{\text{ion}}$  into SIMFAST21, we will average over many halos in each cell which will reduce the scatter further, therefore the scatter

is unlikely to systematically impact the 21-power spectrum. Qualitatively, introducing scatter in  $R_{\text{ion}}$  would introduce larger HII bubbles in diffuse regions and smaller ones in overdense ones, blurring the effect of the  $R_{\text{ion}}$  dependence on  $M_h$  and suppressing large-scale fluctuations. These effects are likely to be small given the small scatter, which only increases substantially at the lowest masses that (we will show later) are not driving reionisation. The key goal of the current work is to improve on previous work by allowing  $R_{\text{ion}}$  to vary with halo mass in a physically-motivated way rather than assuming a constant value. We therefore defer a detailed investigation into the impact of scatter to future work.

To check if these simulated values for  $R_{\text{ion}}$  are reasonable, we compare to the SFR inferred from observations using abundance matching by Behroozi et al. (2013), shown as the dark red vertical error bars at  $10^{11} M_\odot$  (this is the lowest halo mass at which they computed the SFR). To convert from SFR to  $R_{\text{ion}}$ , we invert the process described above, assuming a metallicity corresponding to the mean metallicity of star-forming gas at that epoch. The agreement is within the quoted uncertainty by Behroozi et al. (2013), but in detail we see that our hydrodynamic simulations (**6/256-RT**, **32/512**) produce an  $R_{\text{ion}}$  that is higher by a factor  $\times 1.5$  compared to that inferred by Behroozi et al. (2013). We will return to this point in §4.1.

To implement  $R_{\text{ion}}$  into SIMFAST21, we construct a fitting function for  $R_{\text{ion}}(M_h, z)$  whose mass dependence is analogous to a Schechter function, namely a power-law on one end and an exponential cutoff on the other, and whose redshift dependence is as a power law in the scale factor<sup>7</sup>, namely:

$$\frac{R_{\text{ion}}}{M_h} = A(1+z)^D (M_h/B)^C \exp(-(B/M_h)^{3.0}). \quad (2)$$

We perform a minimization to determine the best-fit parameters to be  $A = 1.08 \times 10^{40} \text{M}_\odot^{-1} \text{s}^{-1}$ ,  $B = 9.51 \times 10^7 M_\odot$ ,  $C = 0.41$  and  $D = 2.28$ . Note that equation (2) shows that  $R_{\text{ion}}$  scales as  $M_h^{1.41}$ , which is consistent with the SFR– $M_h$  relation that previously found by Finlator et al. (2011).

We note that at low redshifts (e.g. today), the high-mass end of  $R_{\text{ion}}(M_h)$  would likely have a sharp turn-down owing to quenching of star formation in  $M_h \gtrsim 10^{12} M_\odot$  halos (e.g. Gabor et al. 2012). We do not produce such large halos by  $z = 6$  in these hydro simulations, although it is possible that our SIMFAST21 volume will be sufficiently large to yield halos above this mass. Nonetheless, there are suggestions that the quenching mass scale is higher at high redshifts (e.g. Dekel et al. 2009; Gabor et al. 2014). For instance, the best-fit parameterisation of the equilibrium galaxy formation model in Mitra et al. (2015) suggests that at  $z = 6$ , the quenching mass scale is close to  $M_h \sim 10^{15} M_\odot$ , which is larger than any halo existing during the EoR. Hence we ignore the possibility of a high-mass turn-down in  $R_{\text{ion}}$  for now.

<sup>7</sup> This is also taken from Francisco et al (2014), where a similar formula used to parameterize the DLA cross-section; see their eq. (4.4).

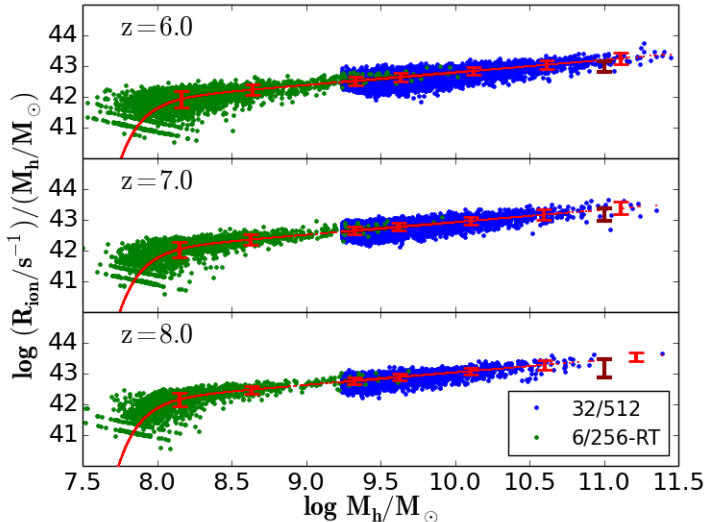


**Figure 1.** Ionization rate  $R_{\text{ion}}$  computed from **6/256-RT** (blue dots) and **32/512** (green) simulations. The overlap between **6/256-RT** and **32/512** simulations occurs in the halo mass range of  $10^{9.3-10} M_{\odot}$ , and the two simulations yields similar results there. The red dots are computed using our fitting function, Equation (2). The red vertical error bars represent  $\sigma$  values for  $\log M_h$  bin size of 0.5. The scatter is fairly small, so is unlikely to systematically impact the 21-power spectrum. The dark red vertical error bars at  $10^{11} M_{\odot}$  are computed using SFR measurements from Behroozi et al. (2013). Our fitting function nicely reproduces the ionisation rate  $R_{\text{ion}}$  computed from our hydrodynamic simulations and only higher by a factor of  $\times 1.5$  than Behroozi et al. (2013) observations.

### 3.2 Recombination Rate, $R_{\text{rec}}$

Since the recombination rate  $R_{\text{rec}}$  depends on the density field and its clumping, we choose to parameterise  $R_{\text{rec}}$  per unit volume in terms of the local scaled density  $\Delta \equiv \rho/\bar{\rho}$ , where  $\rho$  is the matter density and  $\bar{\rho}$  is the cosmic mean at that redshift. Then in SIMFAST21, we can apply this recombination rate to individual cells where we can compute the scaled density. Also, because we want to characterise the inhomogeneous recombination rate during the EoR, we can only use the full radiative hydrodynamic simulation for this, namely **6/256-RT**, and we do not employ the **32/512** run here. Unfortunately, this limits our dynamic range and requires a larger extrapolation to cover the range of overdensities that are achieved in our large SIMFAST21 volume, which is an unavoidable limitation given computational capabilities.

Since the clumping and hence  $R_{\text{rec}}$  is sensitive to scale (e.g. Finlator et al. 2013), we must choose a particular scale over which to compute  $\Delta$  and hence  $R_{\text{rec}}$ . Here we choose to subdivide our  $6h^{-1}\text{Mpc}$  simulation into 16 cells per side, which yields a cell size of 0.535 Mpc (comoving). This then necessarily fixes the cell size that we will use for our SIMFAST21 runs to a value that enables us to feasibly simulate sufficiently large volumes for computing the 21-cm power spectrum on the scales of relevance for current and upcoming observations. We smooth the mass of each gas particle onto these cells using a 5th-order B-spline kernel

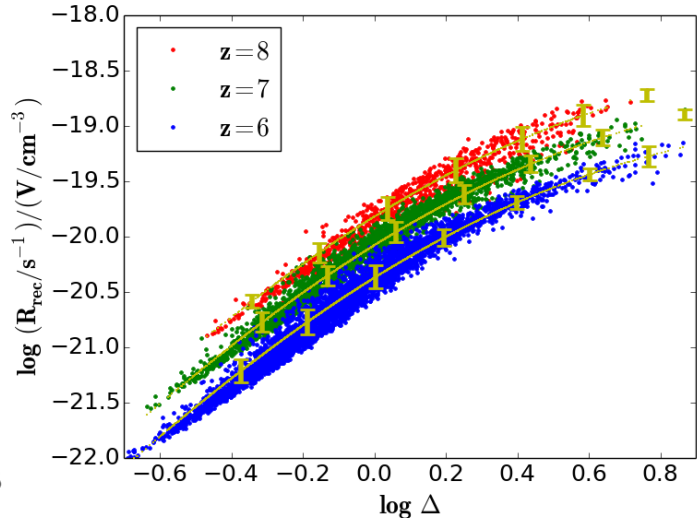


**Figure 2.** Recombination rate density  $R_{\text{rec}}/V$  computed from **6/256-RT** simulation at  $z=6$  (blue-dots),  $z=7$  (green-dots) and  $z=8$  (red-dots). Yellow dots show our fitting function, Equation (4). Vertical error bars represent  $1\sigma$  values for  $\log \Delta$  bin size of 0.2. The scatter is fairly small, so is unlikely to systematically impact the 21-power spectrum. It is quite clear that our fitting function fairly reproduces the recombination rate  $R_{\text{rec}}$  that is computed from our hydrodynamic simulations.

with 128 neighbours as utilised in the **6/256-RT** simulation (Finlator et al. 2015).

Within each so-defined cell in the **6/256-RT** simulation, we compute the volume-averaged recombination rate density,  $R_{\text{rec}}/V$ , as follows:

$$R_{\text{rec}}/V = \alpha_a \langle n_{\text{HII}} n_e \rangle_V / x_i, \quad (3)$$

where  $n_{\text{HII}}$  is ionized hydrogen number density,  $n_e$  is the free electrons number density,  $x_i$  is the cell's ionised volume fraction, and  $\alpha_a = 4.2 \times 10^{13} \text{cm}^3 \text{s}^{-1}$ , that corresponds to a temperature of  $10^4 \text{K}$ . We consider case-A recombination following the recent paper by Kaurov & Gnedin (2014), where it has been shown that case-A recombination photons mimic the scenario of those photons redshifted out of resonance, and therefore can no longer be ionising photons. We compute equation (3) only in cells above a specific ionisation threshold  $x_i > 0.95$ . This is because in our model, SIMFAST21 assumes that ionisations must overcome recombinations in fully ionized medium, once the ionisation condition is satisfied (eq. 5). Therefore, we want to make sure the recombinations rates computed from **6/256-RT** correspond to similarly ionised regions. Then we divide by  $x_i$  in equation (3) to correct for the residual neutral fraction.

Figure 2 shows the recombination rates per unit volume as a function of  $\Delta$  at  $z=6, 7, 8$ . The yellow vertical error bars represent the  $1\sigma$  scatter in bins of  $\log \Delta = 0.2$ . At the mean density ( $\Delta = 0$ ), the scatter is  $\sigma \sim 0.1$ , and is similar for different redshifts and  $\Delta$ . We do not expect that this small scatter will have a significant impact on the derived 21-cm power spectrum. In general,  $R_{\text{rec}} \propto \Delta^2$  as expected since recombination is a two-body process, though there is a slight flattening at high- $\Delta$ . Recombination rates are also higher at higher  $z$ , since the Universe is denser.

We now determine a fitting function for the recombi-

Simulation	Size ( $h^{-1}$ Mpc)	No of Cells	Resolution ( $h^{-1}$ Mpc)
SIMFAST21	210	560 <sup>3</sup>	0.375
<b>6/256-RT</b>	6	16 <sup>3</sup>	0.375
<b>32/512</b>	32	-	-

**Table 1.** shows a summary of our simulations. We use **6/256-RT** simulation to computing both  $R_{\text{rec}}$  and  $R_{\text{ion}}$ . We consider the **32/512** simulation only to computing  $R_{\text{ion}}$ , and hence we don't divide the simulation box into cells.

nation rate density,  $R_{\text{rec}}/V$ . We construct a fitting function  $R_{\text{rec}}/V(\Delta, z)$  as follows:

$$\frac{R_{\text{rec}}}{V} = A(1+z)^D \left[ \frac{(\Delta/B)^C}{1 + (\Delta/B)^C} \right]^4, \quad (4)$$

and we determine the best-fit values to be  $A = 9.85 \times 10^{-24} \text{cm}^{-3} \text{s}^{-1}$ ,  $B = 1.76$ ,  $C = 0.82$ ,  $D = 5.07$ . Note that the redshift dependence is slightly weaker than the expected  $(1+z)^6$  owing to the evolution of the clumping factor (Finlator et al. 2013). Although these fitting values are only applicable for the cell size that we have chosen, namely  $0.375h^{-1}\text{Mpc}$ , we find that re-binning the hydrodynamical simulation using cells that are half as wide leads to an  $R_{\text{rec}}$  that is indistinguishable from our current fit. Furthermore, re-running our reionization simulations with smaller cells but otherwise the same parameters leads to essentially indistinguishable results. Hence our results are not sensitive to this choice of cell size.

Equation (4) thus effectively accounts for the local clumping factor from the **6/256-RT** simulation, that we can implement into a SIMFAST21 simulation where such clumping cannot be resolved. We can thus compute the recombination rate  $R_{\text{rec}}$  in SIMFAST21 by multiplying the recombination rate density  $R_{\text{rec}}/V$  by the SIMFAST21 cell volume.

### 3.3 Modifying SIMFAST21 to use $R_{\text{rec}}$ and $R_{\text{ion}}$

To apply the fitting formulae for  $R_{\text{rec}}$  and  $R_{\text{ion}}$  in SIMFAST21, we first smooth the generated density field. The density field moves relative to the fixed SIMFAST21 grid cells as a consequence of applying the Zel'Dovich (1970) approximation. We must then smooth the density field onto the grid cells during the evolution. Here we implement cloud-in-cell (CIC) smoothing, where each cell contributes to 8 neighbouring cells. We then apply the  $R_{\text{rec}}$  fitting formula (eq. 4) to the CIC-smoothed density field to generate our recombinations rate boxes. For  $R_{\text{ion}}$ , we compute the CIC smoothing directly on the ionisation field that is generated using the halo catalogs via Equation (2).

Given  $R_{\text{ion}}$  and  $R_{\text{rec}}$  computed on the SIMFAST21 grid, we can now use this information to develop a new criterion for whether a particular region is neutral or ionised. To do so, we simply compare the local ionisation rate with recombination rate, and assign the bubble cells to be ionised if:

$$f_{\text{esc}} R_{\text{ion}} \geq R_{\text{rec}}, \quad (5)$$

where  $f_{\text{esc}}$  is our assumed escape fraction. This replaces our previous criterion based on the efficiency parameter  $\zeta$  (eq. 1).

We note that this criterion assumes that, once a particular region satisfies this criterion, it is quickly able to ionise

the vast majority of its neutral gas. This is an approximation, but one expects that the increasing rate of ionising photon production in the early Universe together with the dropping cosmic density will in general yield a fast transition to being fully reionised. Indeed, such a quick transition is typically seen for entire simulation volumes (e.g. Gnedin 2000, and we will later show this for our models as well), and it is physically reasonable to expect such rapid reionisation will also occur locally. To rigorously assess its validity we would need to do a full radiative transfer simulation, which we leave for future work.

In the original SIMFAST21, an ionised cell was set to  $x_{\text{HII}} = 1$ . In reality, even a fully-reionised patch of the Universe has some small residual neutral fraction  $f_{\text{resid}}$ , which depends on the global ionising background and overdensity (Hui & Gnedin 1997). Hence when our ionisation criterion (eq. 5) is satisfied, we set the ionisation fraction to  $x_{\text{HII}} = 1 - f_{\text{resid}}$ , otherwise we leave it as  $x_{\text{HII}} = 0$ .

We calculate  $f_{\text{resid}}$  as follows. First, we obtain the HI photoionisation rate  $\Gamma_{\text{HI}}$ , which corresponds to the flux of ionising photons, from Haardt & Madau (2012). Then, we compute the neutral fraction based on ionisation equilibrium following Popping et al. (2009), which results in

$$f_{\text{resid}} = \frac{2C + 1 - \sqrt{(2C + 1)^2 - 4C^2}}{2C}, \quad (6)$$

with

$$C = \frac{n\beta(T)}{\Gamma_{\text{HI}}}, \quad (7)$$

and where  $n$  is the hydrogen number density,  $T$  is the gas temperature, and the recombination rate coefficient  $\beta(T)$  function (Verner & Ferland 1996) is given by

$$\beta(T) = a \left[ \sqrt{T/T_0} (1 + \sqrt{T/T_0})^{1-b} (1 + \sqrt{T/T_1})^{1+b} \right]^{-1}. \quad (8)$$

For neutral hydrogen, the best-fit parameters are  $a = 7.982 \times 10^{-11} \text{cm}^3 \text{s}^{-1}$ ,  $b = 0.7480$ ,  $T_0 = 3.148 \text{K}$ , and  $T_1 = 7.036 \times 10^5 \text{K}$ . We assume a temperature of  $T = 10^4 \text{K}$  at all times, since  $f_{\text{resid}}$  is only important at the end of reionisation where the universe becomes optically thin.

At the tail end of reionisation, this results in a non-zero  $x_{\text{HII}}$ , unlike in the original code. We note that this is not a direct prediction of this simulation, since it scales with the  $\Gamma_{\text{HI}}$  that we are taking from Haardt & Madau (2012) rather than predicting directly from the model. In the future we plan to do this more self-consistently, but since this has no effect for predicting the 21-cm power spectrum at epochs where reionisation is far from complete, for the present purposes our current prescription is sufficient.

To summarize, we have modified SIMFAST21 to employ the criterion specified in Equation (5) in order to determine whether a given region is ionised. This requires computing the local ionisation photon rate  $R_{\text{ion}}$  (eq. 2) and local recombination rate  $R_{\text{rec}}$  (eq. 4) in each cell, as well as assuming an escape fraction  $f_{\text{esc}}$  that we constrain in the next section. Ionised cells are set to have a residual neutral fraction (eq. 6). Finally, the density field for computing  $R_{\text{rec}}$  and ionisation fields are smoothed using a CIC approach. This completes the SIMFAST21 modifications that we outlined in §2.1, and we will investigate how these changes impact the evolution of reionisation and the 21-cm power spectrum in §5.

## 4 RESULTS FOR OBSERVABLES

### 4.1 Constraints on the photon escape fraction $f_{\text{esc}}$

Our key free parameter is the escape fraction  $f_{\text{esc}}$  of ionising photons from galaxies.  $f_{\text{esc}}$  is essentially set by the amount of recombinations in the ISM that destroy ionising photons, along with dust extinction (Kaurov & Gnedin 2015). Past large-scale models of the EoR typically constrain  $f_{\text{esc}}$  using observations, particularly the Thomson optical depth  $\tau$  from the CMB measurements and  $\text{Ly}\alpha$  observations (Fan et al 2006). Up until recently, most of these models required high  $f_{\text{esc}}$  values to match the observations. As an example, the **6/256-RT** simulation requires an  $f_{\text{esc}}$  that reaches close to unity at high redshifts and small halo masses. However, the new  $\tau$  values from Planck (2015) have eased such constraints, so for instance the semi-analytic model of Mitra et al. (2015) finds that they can match observations with  $f_{\text{esc}} \lesssim 20\%$  throughout the EoR.

An alternative approach to constraining  $f_{\text{esc}}$  is to use extremely high-resolution hydrodynamic simulations to directly predict the escape of ionising photons from the ISM of primeval galaxies. Early simulations by Gnedin et al. (2008) predicted  $f_{\text{esc}} \sim 1 - 3\%$ . First galaxy simulations by Wise et al. (2014) predicted that  $f_{\text{esc}}$  drops from 50% to 5% over halo masses from  $10^7 - 10^{8.5} M_{\odot}$ . Ma et al (2015) used cosmological zoom simulations of more sizable halos to estimate  $f_{\text{esc}} \sim 0.001 - 0.02$  with an average  $f_{\text{esc}} < 5\%$ , with no strong dependence on galaxy mass or redshift. Overall, it appears that direct predictions of  $f_{\text{esc}}$  tend to favor modest values of the order of a few to ten percent in hydrogen cooling halos. While such  $f_{\text{esc}}$  values were difficult to reconcile with previous measurements of  $\tau$ , Robertson et al (2015) noted that the new Planck (2015)  $\tau$  alleviates these tensions.

Here we tune our  $f_{\text{esc}}$  to match a suite of EoR observations. In particular, we will constrain to observations of the Thomson optical depth ( $\tau$ ) to the surface of last scattering from Planck (2015), ionizing emissivity density measurements by Becker & Bolton (2013), and the volume-averaged neutral fraction by Becker & Bolton et al (2015); Fan et al (2006). The measure of  $\tau$  primarily constrains the epoch of onset of reionisation, while the latter two observations primarily constrain the ionising photon budget at the end of the EoR or shortly after. Hence matching all three data sets simultaneously is a significant challenge for models (e.g. see Finlator et al. 2011, 2015; Kuhlen & Faucher-Giguère 2012; Mitra et al. 2011, 2012, 2013).

We begin by assuming a constant  $f_{\text{esc}}$  independent of halo mass or redshift. It is important to note that for our SIMFAST21 runs, this can be regarded as the mean escape fraction from all ionising sources within  $0.375h^{-1}\text{Mpc}$  cells which will typically contain a large number of star forming galaxies; we cannot constrain how  $f_{\text{esc}}$  varies for individual galaxies within each cell. Finlator et al. (2015) found that, to match the previous WMAP optical depth while still finishing reionisation by  $z \sim 6$  required having a strongly mass- and redshift-dependent  $f_{\text{esc}}$ . However, the larger SIMFAST21 volume and the more recent Planck  $\tau$  measurement alters such requirements.

We perform a SIMFAST21 run in a 300 Mpc (comoving) volume with  $560^3$  cells, using our modified version including the  $R_{\text{ion}}$  and  $R_{\text{rec}}$ . We then vary the  $f_{\text{esc}}$  value in order to match  $\tau = 0.066$  from Planck. We are able to match

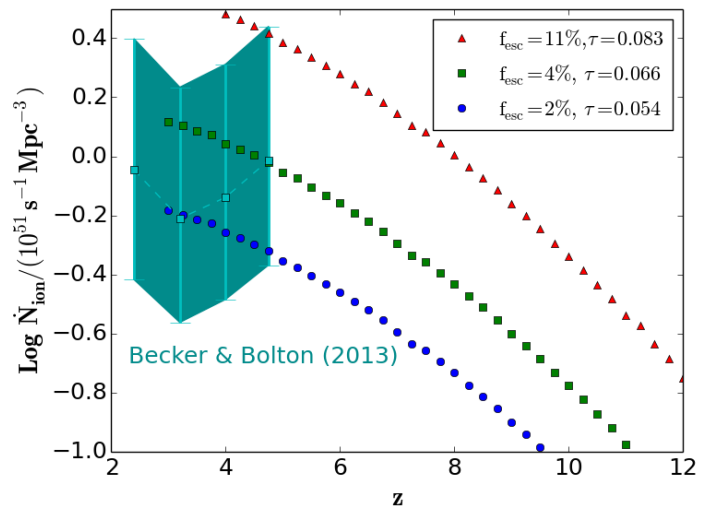


**Figure 3.** The predicted evolution of the ionizing emissivity density from our fiducial model using the  $R_{\text{ion}}$  parametrization, Equation(2). The blue circles, green squares and red triangles represent the ionizing emissivity density of the **Full** model using  $f_{\text{esc}} = 2\%$ ,  $4\%$ , and  $11\%$  respectively. The darkcyan shaded area comes from Becker & Bolton (2013). It is clearly shown that the three chosen values of  $f_{\text{esc}}$  matches the actual, upper and lower limits of the ionizing emissivity by Becker & Bolton (2013) as well as the corresponding recent bounds on the reionisation optical depth  $\tau$  by Planck (2015).

this with  $f_{\text{esc}} = 0.04$ . For comparison, changing  $f_{\text{esc}} = 0.11$  results in a predicted  $\tau = 0.083$  which is the  $1\sigma$  upper limit from Planck, while  $f_{\text{esc}} = 0.02$  results in a predicted  $\tau = 0.054$  which is their  $1\sigma$  lower limit. Hence from this data alone, we constrain  $f_{\text{esc}} = 4_{-2}^{+7}\%$ .

We now examine the predicted ionising emissivity, which is the average rate of ionizing photons emission per unit volume, as measured from the  $\text{Ly}\alpha$  forest at redshifts just after reionisation. To compute this, we extend our SIMFAST21 simulation to lower- $z$ , and we sum the total ionising photon rate  $R_{\text{ion}}$  in all cells at a given redshift and divide by the simulation volume.

Figure 3 shows the predicted values from our simulations as the red, green, and blue dots for  $f_{\text{esc}} = 0.11, 0.04, 0.02$ , respectively. The observational range from Becker & Bolton (2013) is shown as the cyan region. It is clear that  $4\%$  provides a good fit to the observations, particularly at  $z \approx 5$  where our simulations are most valid. We note that this low value of our  $f_{\text{esc}} = 0.04$  has been previously found using a semi-analytic model by Kulkarni et al. (2013). Coincidentally, the  $f_{\text{esc}}$  values to match the upper and lower limits of Planck are comparable to that required to match the upper and lower limits of the ionising emissivity measures, showing that these data sets currently provide comparable constraints on  $f_{\text{esc}}$  for our simulations.

As a final test, we examine the evolution of the cosmic volume-weighted neutral fraction, as can be probed observationally using the opacity of the  $\text{Ly}\alpha$  forest (e.g. Fan et al 2006). This is shown in Figure 4. Focus for now on the solid blue line labeled “**Full**”, which is the model we are considering here with  $f_{\text{esc}} = 0.04$ . In this simulation, the Universe reionises at  $z \sim 7$ . This may be slightly higher than that



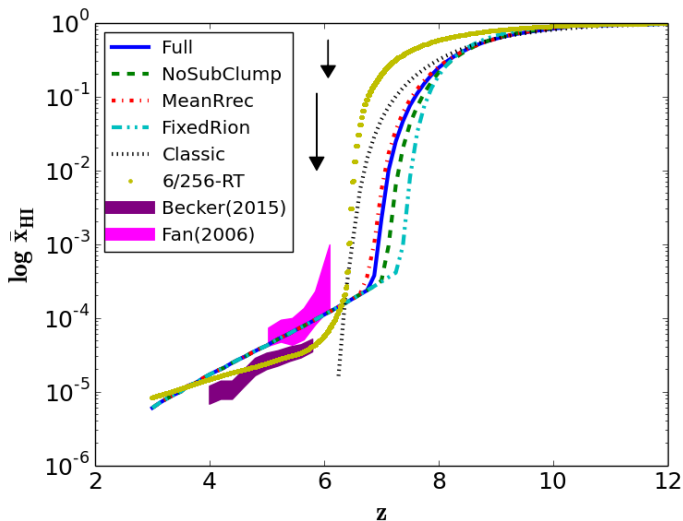


**Figure 4.** The volume-weighted average neutral fraction,  $\bar{x}_{\text{HI}}$ , of our models compared to 6/256-RT (Finlator et al. 2015) and observations. Solid blue represents our fiducial model, **Full**. The **NoSubClump** (Dashed, Green), **MeanRrec** (Dash-dotted, Red), **FixedRion** (Dash-dot dotted, Cyan), **Classic** (Dotted, Black) and **6/256-RT** (Dots, Yellow) are also shown. The shaded magenta and purple show Fan et al (2006) and Becker & Bolton et al (2015) measurements respectively. Vertical arrows represents the recent upper limit constraints by McGreer et al. (2015) at  $z=6$  using  $\text{Ly}\alpha$  and  $\text{Ly}\beta$  forests. It is quite clear that adding the residual neutral  $f_{\text{resid}}$  (eq. (6)) to our fiducial simulations is crucial to match the observation, as opposed to the **Classic** model.

inferred from observations by Fan et al (2006), but there is some uncertainty on this owing to the large sightline-to-sightline variation in the mean  $\text{Ly}\alpha$  opacity (Becker & Bolton et al 2015). Hence we find that a 4% escape fraction is also broadly consistent with observations of the completion of reionisation.

For a more pictorial view, the evolution of the neutral fraction in our fiducial simulation with  $f_{\text{esc}} = 0.04$  is depicted in Figure 5. This shows a one-cell-thick ( $0.375h^{-1}\text{Mpc}$ ) map of the neutral fraction  $x_{\text{HI}}$  (Figure 5) constructed by splicing together the outputs at different redshifts into a continuous series. Reionisation begins at  $z \sim 17$  and the Universe is reionised by  $z \sim 7$ . In our model, the EoR is an extended process since the neutral fraction  $x_{\text{HI}}$  drops slightly from 0.99 to 0.92 as  $z \sim 17 \rightarrow 11$ . It is seen that the ionised gas forms bubbles of increasing size, corresponding to a classic inside-out topology where the densest regions are ionised first<sup>8</sup>. While illustrative, for actually computing the 21-cm power spectrum we will not use the light cone in Figure 5 but rather individual snapshots at various redshifts, since it has been shown by La Plante et al. (2014) that the light cone effect are small for our box size. The goal of the redshifted 21-cm EoR observations is

<sup>8</sup> We note that SIMFAST21 essentially assumes such a topology, since it calculates the ionisation state within bubbles, and assumes that all the gas within a bubble is fully ionised; it is not possible to get neutral patches within such bubbles that would correspond to outside-in reionisation.

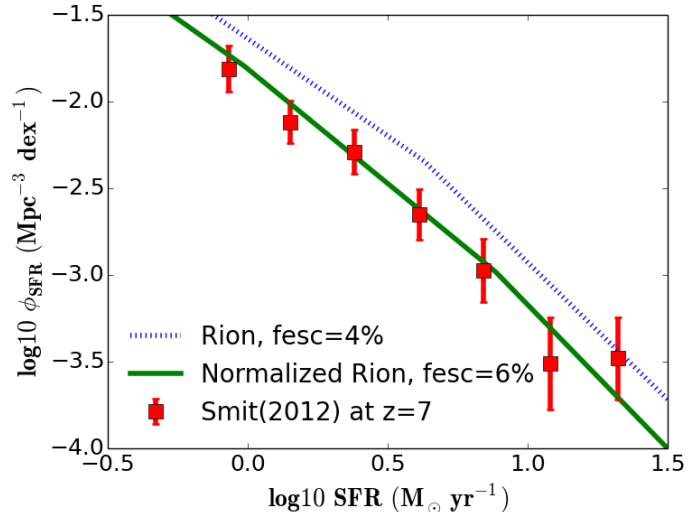


**Figure 6.** Comparison of the SFR functions from our SIMFAST21 using  $R_{\text{ion}}$  (blue, dotted-line) with the stepwise SFR functions of Smit et al. (2012) which were derived from the dust-corrected UV Luminosity functions. The SFR at a given halo mass from SIMFAST21, using  $R_{\text{ion}}$  from hydrodynamic simulations (**6/256-RT**, **32/512**), is higher by a factor of  $\times 1.5$  than implied by observations. The green solid line shows the SFR function from SIMFAST21 using the normalized  $R_{\text{ion}}$  that matches Smit et al. (2012).

to constrain this bubble size distribution and its evolution through measurements of the power spectrum, thereby providing constraints on the topology and sources of reionisation.

As noted earlier in Figure 1, it appears that the global ionisation rate, and by proxy the star formation rate, at a given halo mass in our hydrodynamical simulations may be high by a factor of  $1.5 \times$  compared to observations. To investigate this in more detail, we show in Figure 6 the star formation rate function from our SIMFAST21 using  $R_{\text{ion}}$  (blue, dotted-line), compared to observations by Smit et al. (2012) at  $z = 7$ . Indeed, we see that our simulated SFRs are generally higher by this factor across all galaxies.

Given that this discrepancy is mostly invariant with star formation rate, for the purposes of EoR modeling it can be directly translated into a correction factor on the escape fraction. In other words, if we corrected our  $R_{\text{ion}}$  values down by a factor of 1.5 (normalized  $R_{\text{ion}}$ ) to account for the mismatch in SFRs (green solid line in Figure 6), we could raise our  $f_{\text{esc}}$  values by a factor of 1.5 and obtain the exact same results for the 21 cm power spectrum (see Figure 13); there is no impact on the predicted power spectrum of 21-cm fluctuations for a model whose  $f_{\text{esc}}$  is tuned to match observations of the history of reionization.

Hence if we take the observations of Smit et al. (2012) at face value, we require an escape fraction of  $6_{-3}^{+10.5}\%$  to match the various EoR observations described above. This would alleviate some of the discrepancy between our value and that inferred by Robertson et al (2015), who argued for  $f_{\text{esc}} = 20\%$  from observations. At the same time, it is not in conflict with direct observational constraints on  $f_{\text{esc}}$ , which tend to prefer values of less than 10%.

To summarize, our simulation with the new version of SIMFAST21 yields the somewhat remarkable result that

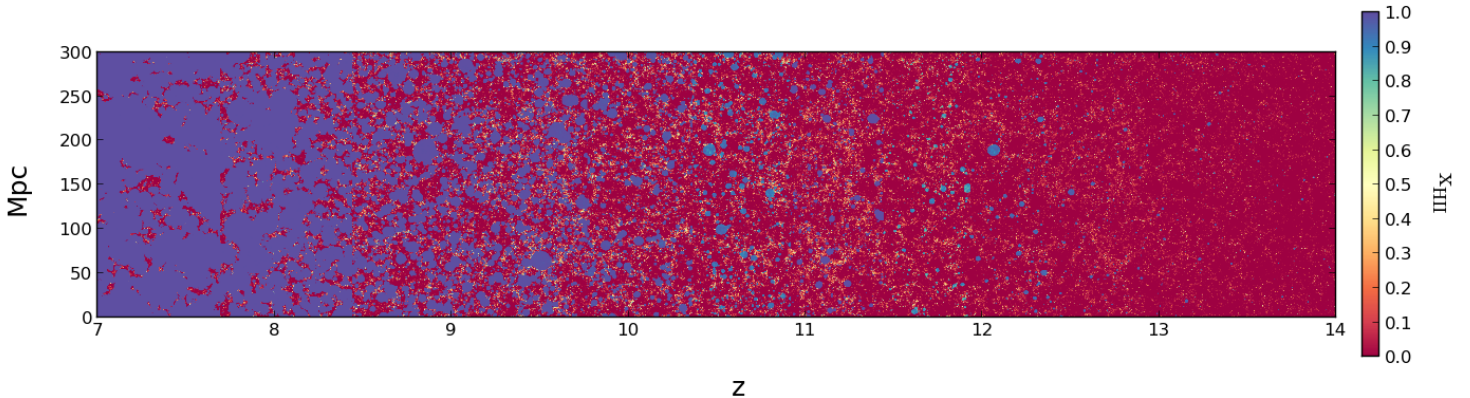


**Figure 5.** Evolving map of the neutral fraction in our 300 Mpc,  $560^3$  cell SIMFAST21 simulation with a 4% escape fraction.

a constant escape fraction of 4%, independent of mass or redshift, is sufficient to match observational constraints on both the onset and end of reionisation. This value may be increased to 6% when we fine-tune our model to match observed star formation rate measurements of Smit et al. (2012) using the normalized  $R_{\text{ion}}$ . Robertson et al. (2015) also argued for a relatively modest escape fraction ( $f_{\text{esc}} = 20\%$ ) based on the new Planck  $\tau$ , which is somewhat higher than our preferred value. In contrast, previous works such as Finlator et al. (2015) have argued for a substantially varying, and generally much higher,  $f_{\text{esc}}$ . Even if we constrain to the WMAP  $\tau = 0.078$ , we still require an escape fraction of only  $\approx 20\%$ , still much lower than Finlator et al. (2015); hence it is not only just the new value of  $\tau$  that is driving our lower  $f_{\text{esc}}$ . Additionally, the key aspect is the large volume of the SIMFAST21 simulation that includes more massive halos relative to small-volume, full-RT simulations. We will show in §5.4 that, in our new SIMFAST21 model, these moderate-mass halos are an important contributor to the photon budget, because the ionising photon rate scales super-linearly with halo mass (eq. 2). This highlights the importance of running large-volume simulations, tuned to available observations, to properly characterise the escape fractions that are required to complete reionisation.

#### 4.2 The 21 cm power spectrum

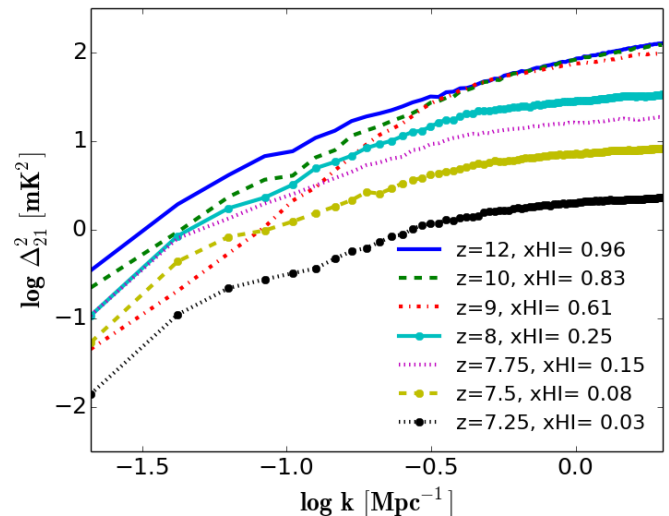
Using our well-constrained SIMFAST21 simulation for the evolution of the ionisation field, we now make predictions for our key observable, namely the redshifted 21-cm power spectrum.

Under the assumption that the spin temperature is much higher than the CMB temperature, we compute the 21-cm brightness temperature as follows:

$$\delta T_b(\nu) = 23x_{\text{HI}}\Delta \left( \frac{\Omega_b h^2}{0.02} \right) \sqrt{\frac{1+z}{10}} \frac{0.15}{\Omega_m h^2} \left( \frac{H}{H + dv/dr} \right) \text{mK}, \quad (9)$$

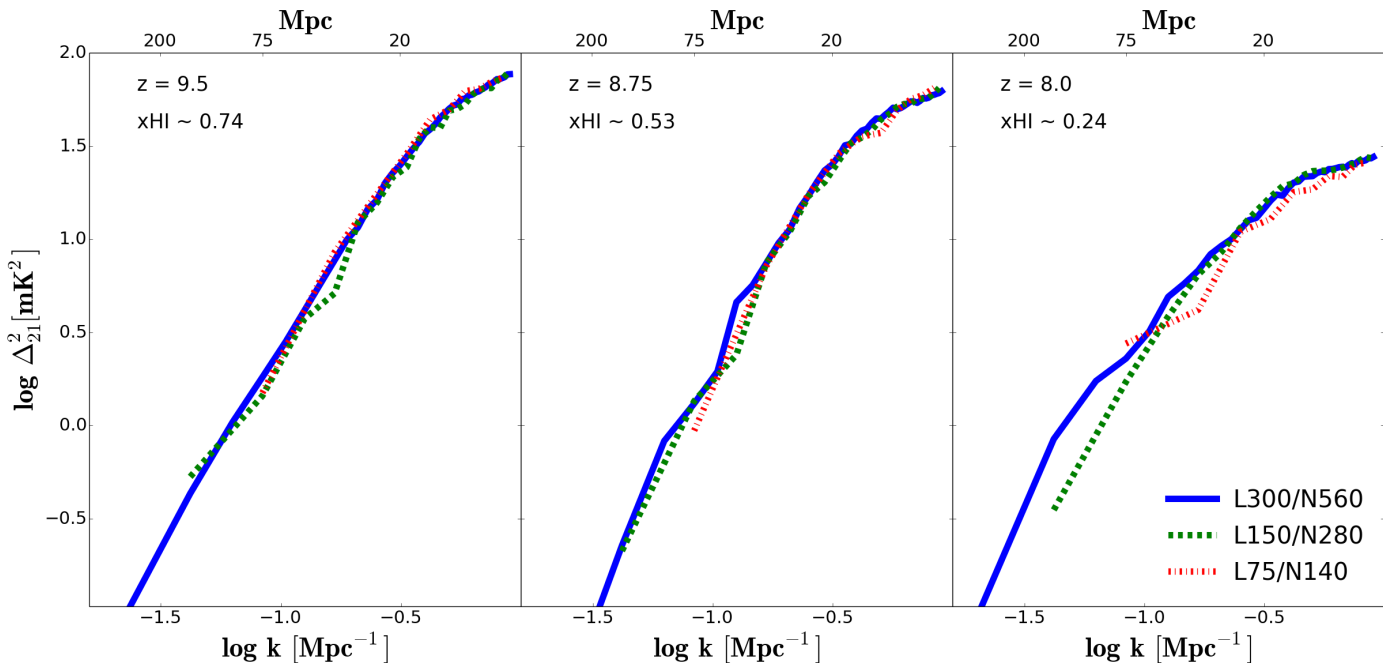
where  $dv/dr$  is the comoving gradient of the line of sight component of the comoving velocity. Using Equation (9), we define the 21-cm power spectrum as follows:  $\Delta_{21}^2 \equiv k^3 / (2\pi^2 V) \langle |\delta T_b(\mathbf{k})|_k^2 \rangle$ .

Figure 7 shows the 21cm power spectrum at  $z=7.25, 7.5, 7.75, 8, 9, 10, 12$  from our 300 Mpc,  $560^3$ -cell SIMFAST21



**Figure 7.** 21-cm power spectrum predicted at  $z=7.25, 7.5, 7.75, 8, 9, 10, 12$  from our fiducial SIMFAST21 run. At early times ( $z=12$ ), the 21-cm power spectrum traces the density field power spectrum. During  $z = 12 \rightarrow 9$ , the presence of more ionised hydrogen in large over-dense regions than under-dense regions suppresses the 21-cm power spectrum. At the intermediate phases, the rapid growth of ionised bubbles boosts the 21-cm power spectrum. At later epochs, when the EoR is nearly complete, the 21-cm power spectrum drops rapidly.

simulation. The evolution in Figure 7 qualitatively follows the pattern described in Lidz et al. (2008): At early times ( $z=12$ ), the 21cm power spectrum traces the density power spectrum, because virtually all of the gas is neutral. During the interval  $z = 12 \rightarrow 9$ , the tendency for reionisation to begin in the largest overdensities offsets the tendency for such overdensities to host high concentrations of neutral gas. As soon as the most overdense regions are ionized, the density field of neutral hydrogen is overall much more homogeneous than prior to reionisation, suppressing large-scale power in 21cm fluctuations. At later epochs, the ionised regions become larger, leading to more large-scale power. In essence, this behavior is reflective of inside-out reionisation where the inhomogeneities are first prominent on smaller scales and then move to larger scales.



**Figure 8.** Volume convergence of the 21-cm power spectrum for SIMFAST21 runs with a box size of 300 Mpc (blue, solid), 150 Mpc (green, dashed), and 75 Mpc (red, dashed-dotted). The convergence at all redshifts is excellent up to about one-quarter of the box size.

As emphasized by Sobacchi & Mesinger (2014), a spatially-inhomogeneous recombination rate suppresses fluctuations on scales larger than  $\sim 0.1 \text{ Mpc}^{-1}$  (this effect is also visible in Figure 1 of Lidz et al. (2008), although they did not emphasise it). The major advance in our work with respect to Lidz et al. (2008) and Sobacchi & Mesinger (2014) and others is a demonstration that including a superlinear dependence of ionising efficiency on halo mass amplifies large-scale fluctuations, partially restoring the flatness of the 21cm power spectrum; we will return to this point in our discussion of Figure 13.

Figure 7 represent our predictions for the evolution of the 21-cm power spectrum from the EoR. In a follow-up paper, we will examine the detectability of  $\Delta_{21}^2$  for ongoing and upcoming 21-cm EoR experiments. For this work, we focus on studying how  $\Delta_{21}^2$  is impacted by the physical modeling variations that we have implemented into SIMFAST21.

### 4.3 Numerical convergence

Our chosen simulation volume is generally limited by our computational capabilities, together with the requirement that our cell size match the chosen cell size over which we have computed our recombination rate in the **16/256-RT** simulation. Here we check whether our results are robust to our choice of volume by running simulations with smaller volumes (keeping the cell sized fixed). This will also allow us to empirically determine the largest robustly predicted scale in our simulation for a given box size.

Figure 8 shows the 21-cm power spectrum  $\Delta_{21\text{cm}}(k)$  calculated from boxes with length 150 Mpc (green, dashed) and 75 Mpc (red, dot-solid), along with our fiducial 300 Mpc box (blue solid). These show  $\Delta_{21\text{cm}}(k)$  over scales from twice the cell size up to the full box size. The corresponding physical

scale  $2\pi/k$  is shown along the top axis. Three panels show  $z = 9.5, 8.75, 8$  which correspond to global neutral fractions of roughly three-quarters, one-half, and one-quarter, respectively.

Generally, the numerical convergence with box size is very good, particularly during the early phases of reionisation. At  $z = 8$ , some deviations are seen at the large scales (small  $k$ ), which start at about one-quarter of the box size or larger, but they are typically less than a factor of 2 in the power. We conclude that our simulations can robustly predict the 21-cm power spectrum over the range of scales from a few times the cell size up to one-quarter of the box size, over the redshift range where there is a significant global neutral fraction and hence 21-cm signal.

## 5 IMPACT OF VARYING IONISATIONS AND RECOMBINATION ASSUMPTIONS

Our main improvement from the previous version of SIMFAST21 is a more physically-motivated characterisation for the ionising source population and small-scale recombinations. Here we quantitatively investigate the impact of these new parameterizations for  $R_{\text{ion}}$  and  $R_{\text{rec}}$  on the reionisation history and morphology, in comparison with previous assumptions. We do so by essentially reverting our new code back towards the original code one piece of physics at a time, so that we can isolate the impact of each new physical component.

To do this, we run five simulations with a box size  $L = 300 \text{ Mpc}$  and  $N = 560^3$  on a side using the same density field and halo catalogs (i.e. the same cosmology), only with different astrophysical assumptions for  $R_{\text{ion}}$  and  $R_{\text{rec}}$ . Because this changes the evolution of the ionisation field, in order to make the comparison more uniform, we re-tune

the photon escape fraction  $f_{\text{esc}}$ , or in the case of the original SIMFAST21 the efficiency parameter  $\zeta$ , in order to achieve the Planck  $\tau = 0.066 \pm 0.016$ . By doing so, we can compare these models at the same redshift and neutral fraction more meaningfully.

The five simulations are as follows:

- **Full**: This is our fiducial model in which we use our new parameterizations  $R_{\text{ion}}$  and  $R_{\text{rec}}$  in Equation (5) to identify the ionised regions, assuming  $f_{\text{esc}} = 4\%$ .

- **NoSubClump**: Similar to **Full**, but using inhomogeneous recombinations computed from local cell’s densities ( $=\alpha_a n_{\text{H}}^2$ ) with no contribution from sub-grid clumping, we re-tune to obtain  $f_{\text{esc}} = 2.5\%$ .

- **MeanRrec**: Similar to **Full**, but using a spatially-homogeneous recombination rate computed from the mean hydrogen cosmological density at each  $z$ ;  $f_{\text{esc}} = 1.5\%$ .

- **FixedRion**: Similar to **Full**, only using Fixed Rion per halo mass  $= 9 \times 10^{49} \text{sec}^{-1}$  which corresponds to the value for  $M_{\text{h}} = 10^8 M_{\odot}$  and assuming  $f_{\text{esc}} = 100\%$ .

- **Classic**: This run with the original SIMFAST21 using Equation(1) to identify the ionised regions with  $\zeta = 11$ .

Our **Full** model is what we have used to make the predictions presented so far. The **NoSubClump** and **MeanRrec** simulations do not use the  $R_{\text{rec}}$  taken from our **16/256-RT** box, but rather compute recombinations locally on a cell-by-cell basis, and globally using the cosmic mean density, respectively. Variations among these three runs can thus be used to isolate the scale at which recombinations are important. The **FixedRion** simulation is analogous to using a constant efficiency parameter, but still uses our **Full** recombination model; hence comparing to the **Full** model can be used to assess the importance of employing a halo mass-dependent ionisation rate. The **Classic** case is the original SIMFAST21 code, which uses a constant efficiency parameter and no explicit recombinations.

We now focus on the variations among these models for the key observables that we have described before, and provide a physical interpretation for the differences that we see.

### 5.1 Global neutral fraction history

Figure 4 shows the volume-weighted neutral fraction ( $\bar{x}_{\text{HI}}$ ) evolution produced by our five models, as labeled. We also show this evolution taken directly from the **6/256-RT** simulation as the yellow dots. Observations by Fan et al (2006) and Becker & Bolton et al (2015), with  $1\sigma$  range, are indicated by the shaded regions. Vertical arrows represents the recent “model-independent” upper limits by McGreer et al. (2015) at  $z = 6$  using the Ly $\alpha$  and Ly $\beta$  forests.

At high- $z$ , the onset of reionisation is similar for all models, primarily because we have tuned them to match the Planck  $\tau$  value which is most directly a constraint on the onset of reionisation. Comparing our **Full** simulation first to the **6/256-RT** simulation, we note that while the shape of  $\bar{x}_{\text{HI}}(z)$  is similar, reionisation occurs earlier by  $\Delta z \sim 0.5$ . As mentioned before, this owes to the small dynamic range of **6/256-RT** that fails to capture: (i) the very earliest stages driven by the rarest over densities corresponding to the longest-wavelength fluctuations. (ii) the larger halos that are important particularly during the later stages of the EoR.

Comparing the **Full** to **Classic** runs, it is seen that the **Classic** run reionises the Universe later, more like  $z \sim 6.5$ . Since this model has no explicit model for recombinations, the early ionisations are very effective, which reduces the amount of ionisations needed at early times in order to reproduce the Planck  $\tau$  value. This results in less ionising photons overall, which delays reionisation. The strength of this effect is best quantified by comparing to the **FixedRion** run, which like the **Classic** case has a constant ionising photon efficiency per unit halo mass. Comparing these we can see that ignoring recombinations can shift the end of the EoR by  $\Delta z \sim 1$ .

The impact of recombinations is seen by comparing the **Full**, **NoSubClump**, and **MeanRrec** models. The differences in the ionisation history are relatively minor, with **NoSubClump** producing slightly earlier reionisation. In this comparison, **Full** and **MeanRrec** produce very similar global reionisation histories, but we will later see they differ significantly in terms of topology.

Overall, changing the nature of the ionisation sources has a larger impact, at fixed  $\tau$ , than varying the recombination methodology. Nonetheless, constraining to match  $\tau$  results in models having an end of reionisation all within  $\Delta z \sim 1$  of each other. Hence the global evolution of the neutral fraction is relatively insensitive to our modifications to SIMFAST21, with the largest difference being relative to a model with no recombinations (**Classic**) or a small-volume hydrodynamic simulation that does not yield large galaxies (**6/256-RT**).

### 5.2 Ionizations Maps

We now explore how the topology of reionisation varies amongst our five different physical models. This is relevant to the 21-cm power spectrum since it focuses on topological features such as the distribution of ionised bubble sizes that directly reflects in the power spectrum. Furthermore, forthcoming observation with the SKA can in principle directly map the neutral gas distribution. To get a flavour for the sorts of topology variations introduced by varying our input physics, we begin by examining maps of the ionisation field evolution.

Figure 9 shows maps of the ionisation field for the five models across different phases of the EoR at  $z = 9.5, 8.75, 8.0$  (top to bottom). Overall, the Universe becomes more ionised at later epochs, and the global neutral fractions are generally similar at the same  $z$ . Nonetheless, there are clear differences in the topology of the ionised regions amongst the various models.

The **Full** and **NoSubClump** models display quite similar morphologies across all EoR phases as seen in their ionisations maps (first two columns). This implies that including the sub-grid clumping effects through  $R_{\text{rec}}$  does not strongly affect the EoR topology, and suggests that computing recombinations using only the local cell’s densities (as in **NoSubClump**) is sufficient to properly model the EoR. This is tantamount to saying that the local clumping factor within each cell is close to unity, and the main variations in the clumping factor occur on scales larger than our cell size; indeed, we have checked that this is the case within the **6/256-RT** run. While this suggests that including  $R_{\text{rec}}$  was perhaps superfluous, this outcome was not obvious from

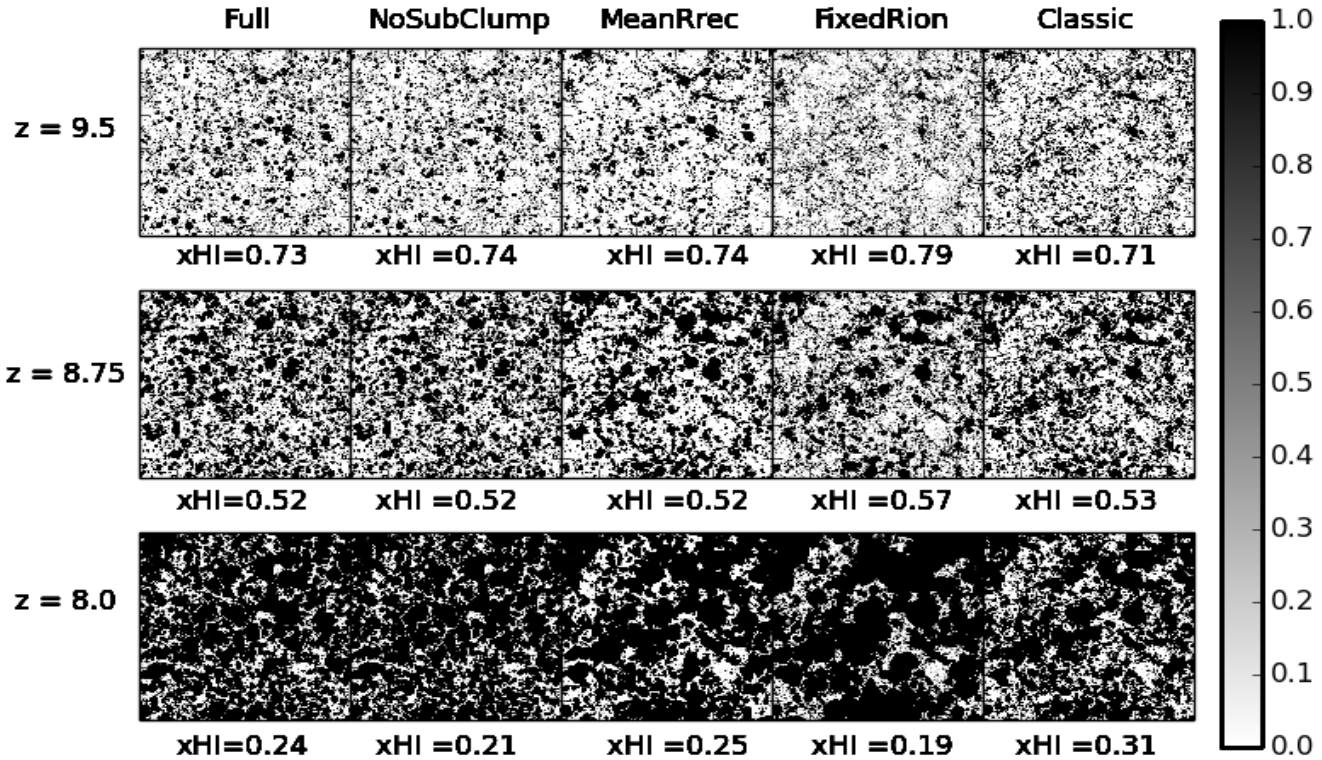


**Figure 9.** The ionisation maps of the five models at  $z=9.5$  (top-row),  $z=8.75$  (middle-row) and  $z=8.0$  (bottom-row). White regions are neutral whereas Black regions are ionized. It is clear that the **Full** and **NoSubClump** models display similar morphologies across all EoR phases, suggesting that the local sub-clumping effects ( $\leq 0.5\text{Mpc}$ ) have no significant contribution to the EoR on large scales ( $\geq 100\text{Mpc}$ ). The **FixedRion**, **MeanRrec** and **Classic** models display similar morphologies only with different bubble sizes due to the variation in the physical assumptions.

the outset. This perhaps conflicts with the conclusions of Raičević & Theuns (2011); their Figure 2 suggests that the local clumping fluctuations are quite important. We then expect that the **Full** and **NoSubClump** models will accordingly produce the same ionisation and 21-cm power spectra.

The **MeanRrec** ionisation maps show relatively larger ionised bubbles (third column) than in our fiducial model. Hence ignoring the density fluctuations and clumping on large scales and assuming recombinations based on the cosmic mean density is a poor approximation. This occurs because the **MeanRrec** model has fewer recombinations, because the recombinations primarily occur in the dense regions, and the recombination rate scales roughly as the square of the density. Therefore, the ionising photons can propagate farther and create larger bubbles.

At early stages of the EoR (at  $z=9.5$ ), the **FixedRion** model (fourth column) produces smaller ionised bubbles than other models. This occurs because of the interplay of recombinations and the ionising source locations. Given that our reionisation topology is generally inside-out (dense regions ionising first), this means that the dense regions with the largest halos live in regions that are most rapidly recombing. In the **Full** model, the increasing strength of ionising

photon output with halo mass helps to offset these rapid recombinations, and power ionising fronts out of the dense regions. However, in the **FixedRion** model the large halos have lower ionising output, and hence the resultant bubbles grow less before stalling. Conversely, in low-density regions with smaller halos, **FixedRion** will produce larger bubbles. Hence overall, the bubble size distribution is more uniform in this case, which will be evident in the power spectra we consider below.

It is interesting to note that the **MeanRrec** and **FixedRion** models share similar morphologies at the intermediate phase of the EoR ( $z = 8.75$ ), which implies that inhomogeneous  $R_{\text{rec}}$  has roughly a similar level of an effect as including mass-dependent ionisation. Given that we have constrained all models to match the *Planck* optical depth, a “crossover” at  $x_{\text{HI}} \sim 0.5$  is perhaps not surprising.

Finally, the **Classic** (fifth column) displays a morphology that is between **FixedRion** and **MeanRrec** morphologies. Its form of ionisation is most similar to **FixedRion**, but it includes recombinations implicitly through the constrained efficiency parameter  $\zeta$  (eq. 1) as a direct suppression of the number of ionising photons output in each cell. Effectively, this cell-based suppression ends up being stronger

than the recombinations in **MeanRrec** and weaker than that in **FixedRion**, which sets the **Classic** morphology between those of **MeanRrec** and **FixedRion**

These results show that assumptions regarding the ionisation and recombination rates in large-scale models can have a significant effect on the topology of reionisation and its evolution.

### 5.3 Ionized mass fraction as a function of density

We now quantify the topology shown in the maps in the previous section. The approach we use here is to consider the ionised mass fraction as a function of local overdensity, to better understand how our physical assumptions are impacting the ionisation state of the gas in various environments.

Figure 10 shows the mass-weighted global ionised fraction  $\bar{x}_m$  as a function of density  $\Delta_{\text{bin}}$  of our five models at three different redshifts  $z = 9.5, 8.75, 8.0$  (left to right), when the neutral fraction is approximately 0.75, 0.5, and 0.25, with some variations between the models (the values quoted on the figure are the average  $x_{\text{HI}}$  of all models at each  $z$ ).

In all models and at all times, the over-dense regions ( $\log \Delta_{\text{bin}} > 0.0$ ), where the halos and hence the photon sources are more numerous, are more ionised while low-density regions such as voids ( $\log \Delta_{\text{bin}} < 0.0$ ) take longer to become ionised. This is due to the gradual progress of the ionisations fronts through the surrounding regions into low density regions (Iliev et al. 2006), and the relatively low clumping factor (Finlator et al. 2013) and recombination rate particularly in the late EoR, which results in these high-density regions remaining ionised. Hence in all these runs, as we saw in the **Full** case earlier (Figure 5), reionisation proceeds in an inside-out fashion.

We first compare **Full** (solid blue) with **NoSubClump** (dashed green). In the moderate and low-density regions, these models are essentially identical, except at late times when the ionised fraction in **NoSubClump** is slightly higher (likely an artifact of tuning to the same  $\tau$  value). Sub-cell gas clumping thus only has an effect in relatively more over-dense regions, which physically makes sense since such clumping occurs on small scales. The impact of sub-cell clumping is maximized at overdensities  $\Delta_{\text{bin}} \sim 5 - 10$ , whereas in the most dense regions the ionisations overwhelm recombinations regardless of the clumping. However, the trend is opposite to one might naively expect: The **NoSubClump** model actually has a lower ionisation fraction, indicating more recombinations, than the **Full** model. This happens because the **NoSubClump** model computes the reionisation rate assuming a fully ionised cell at the cell's density, but the  $R_{\text{rec}}$  fitting formula used in **Full** includes the effect that dense regions have more neutral gas, and hence the recombination rate is lowered compared to the fully ionised case.

Comparing **MeanRrec** to **Full**, we see much more dramatic differences than compared to **NoSubClump**. As we have seen from the maps earlier, assuming recombinations only at the mean cosmic density produces quite a different topology. The ionised fraction is significantly higher in the high-density regions, and lower in the low-density regions, with a crossover around the mean density ( $\Delta = 1$ ). Since recombinations scale as the square of the density, dense re-

gions have lower recombination rates in **MeanRrec** leading to more ionised gas, and conversely low-density regions have higher recombination rates leading to less ionised gas.

The **MeanRrec**, **FixedRion** and **Classic** have roughly the comparable behaviour of  $\bar{x}_m$  during the early phases of the EoR. This also was clear in their topologies (Figure 9). Once these models are constrained to have matching  $\tau$  values which governs their early EoR evolution, using a mean density recombination rate with inhomogeneous sources turns out to be roughly equivalent in topology to using a fixed ionising output per unit mass and inhomogeneous recombinations. The **Classic** model falls in between these two extremes, with fixed ionising efficiency and the recombinations implicitly tied to the ionisations. At lower redshifts, the three models start to diverge at low densities, as the higher recombination rates at  $\log \Delta < 0$  in the **MeanRrec** model lead to lower ionised fractions than in the **FixedRion** model. The **Classic** model is still lower, since the recombinations are tied to ionisations which are very low in the low-density regime. Interestingly, in this regime the **FixedRion** model becomes similar to the **Full** case.

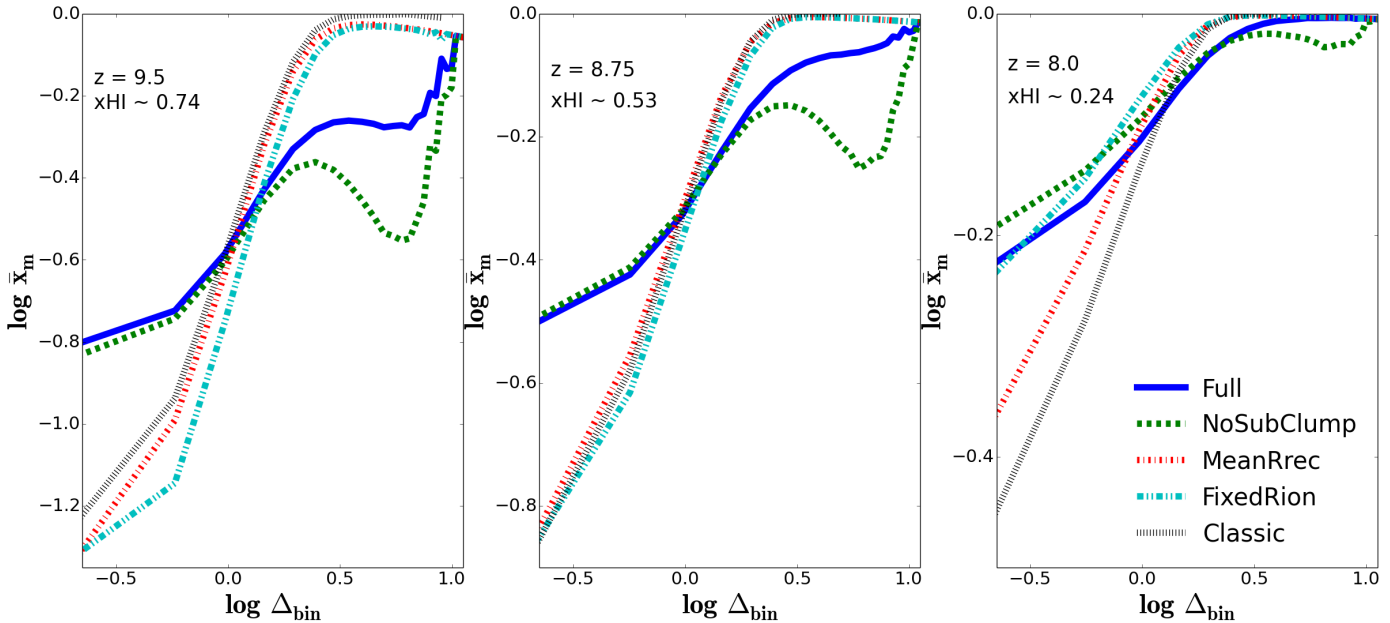
Overall, our results show that including both inhomogeneous recombinations and ionisations is important to produce the correct topology evolution of the EoR. While neglecting sub-cell recombinations has little impact, assuming either recombinations that are based on the mean density or tied to the ionisation rate results in dramatically different ionised gas topologies. Likewise, using a fixed ionising photon output per unit halo mass results in a substantially different topology during the neutral-dominated phase of the EoR, though it becomes more similar to the fiducial case at later stages.

### 5.4 Ionizing photon output versus halo masses

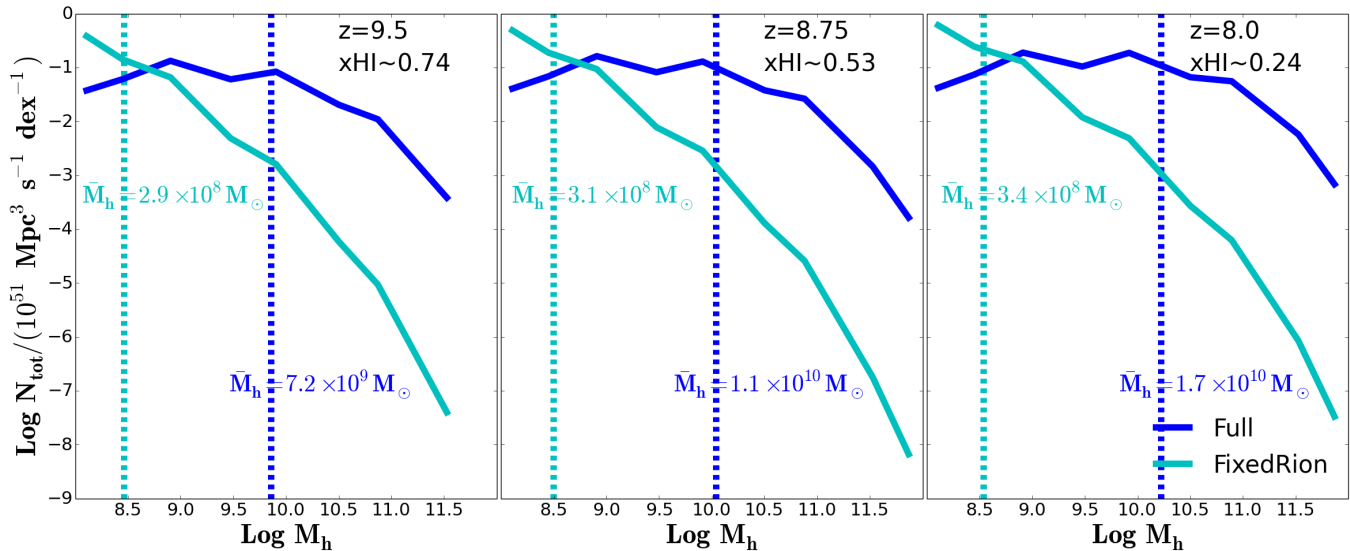
An interesting quantity for observing the EoR is the mass scale of galaxies providing the bulk of the ionising photons. This is important for future observational programs with for instance the *James Webb Space Telescope*, which aims to directly detect these galaxies. Given that we track the ionising output of halos, we can straightforwardly determine the ionising photon distribution as a function of halo mass, and assess the impact of our new input physics on this. We consider only on our fiducial (**Full**) and **FixedRion** models, to compare the total amount of emitted ionising photons per halo mass in each model at fixed  $\tau$ , since we are not concerned with recombinations here.

Figure 11 shows histograms of the total ionising emissivity  $N_{\text{tot}}$  for halo mass bins of the **Full** (blue) and **FixedRion** (cyan) at  $z = 9.5, 8.75, 8$  (from left to right). The **FixedRion** model, with an assumed constant escape fraction and constant ionising output per unit halo mass, results in a steeply declining ionising emissivity with  $M_h$  that mimics the steep halo mass function. In contrast, the **Full** model has greater ionising output per  $M_h$  for more massive halos, shifting the distribution towards higher halo mass.

The vertical dashed lines (blue:**Full**, cyan:**FixedRion**) in Figure 11 represent the ionisation-weighted halo mass  $\bar{M}_h$  of all halos at the corresponding redshifts ( $z=9.5, 8.75, 8.0$ ).  $\bar{M}_h$  thus represents the halo mass limit above (or below) which 50% of the total ionizing photons is being emitted. We see that the  $\bar{M}_h$  is  $\sim 10^{10} M_{\odot}$  in our fiducial model



**Figure 10.** The mass-weighted ionized fraction  $\log \bar{x}_m$  evolution of the five models for given overdensity bin  $\log \Delta_{\text{bin}}$ . LEFT: Early EoR phase, MIDDLE: Intermediate EoR phase and Right: Final EoR phase. The over-dense regions ionize first while the under-dense regions take longer to become ionised, which shows that the EoR proceeds in an inside-out fashion.



**Figure 11.** Total ionizing emissivity ( $N_{\text{tot}}$ ) of our fiducial model (blue, solid) and the **FixedRion** (cyan, solid) for halo mass bin size of 0.5. Vertical dashed lines represent the ionisation-weighted halo mass ( $\bar{M}_h$ ) of the **Full** (blue) and **FixedRion** (cyan) models. It is evident that the dominant halo mass during EoR is much larger in our fiducial model than in the **FixedRion** model by about 1-2 order of magnitude.

whereas it is  $\sim 10^{8.5} M_\odot$  in **FixedRion**, with only a mild dependence on redshift.

Hence a model assuming a fixed ionising output per unit halo mass would predict that reionisation is dominated by extremely small galaxies near the hydrogen cooling limit, while a more realistic model for ionising photon output suggests that moderate-mass halos are responsible for reionisation. The latter scenario bodes well for future direct observations of galaxies driving reionisation, since galaxies in  $\sim 10^{10} M_\odot$  halos are likely to be detectable with *Webb*.

## 5.5 Ionizations and 21-cm power spectra

We now examine how these physical variations impact the ionisation and 21-cm power spectra. The 21-cm power spectrum is the key observable that will be obtained in the forthcoming 21-cm EoR observations. We compute the ionisation power spectrum as  $\Delta_{\text{xx}}^2 \equiv k^3 / |(2\pi^2 V) \langle |x_{\text{HII}}|^2 \rangle / x_{\text{HII}}^2$ , analogous to the 21-cm power spectrum that was introduced in §4.2.

In Figure 12 and 13, we compare the ionization fields

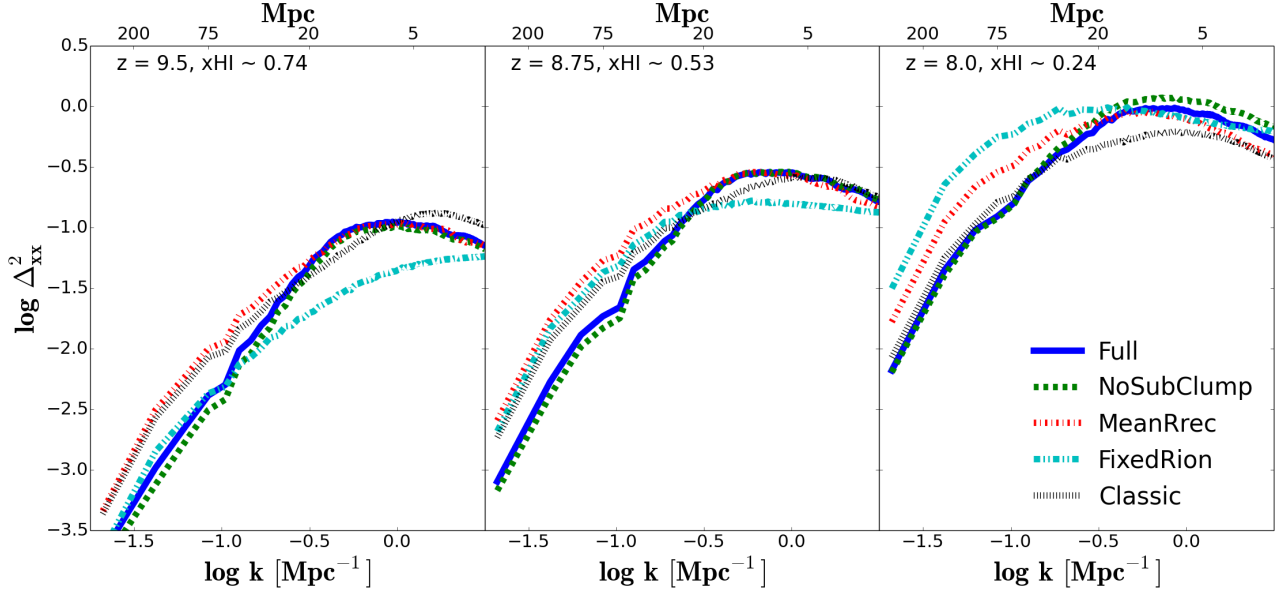


**Figure 12.** The power spectra of the ionisation fields of the five models at different stages during the EoR. Variations in physical assumptions can result in  $\times 2 - 3$  variations in the ionisation power spectrum such as:  $R_{\text{rec}}$  suppresses the large-scale power spectrum while  $R_{\text{ion}}$  boosts the small-scale power spectrum.

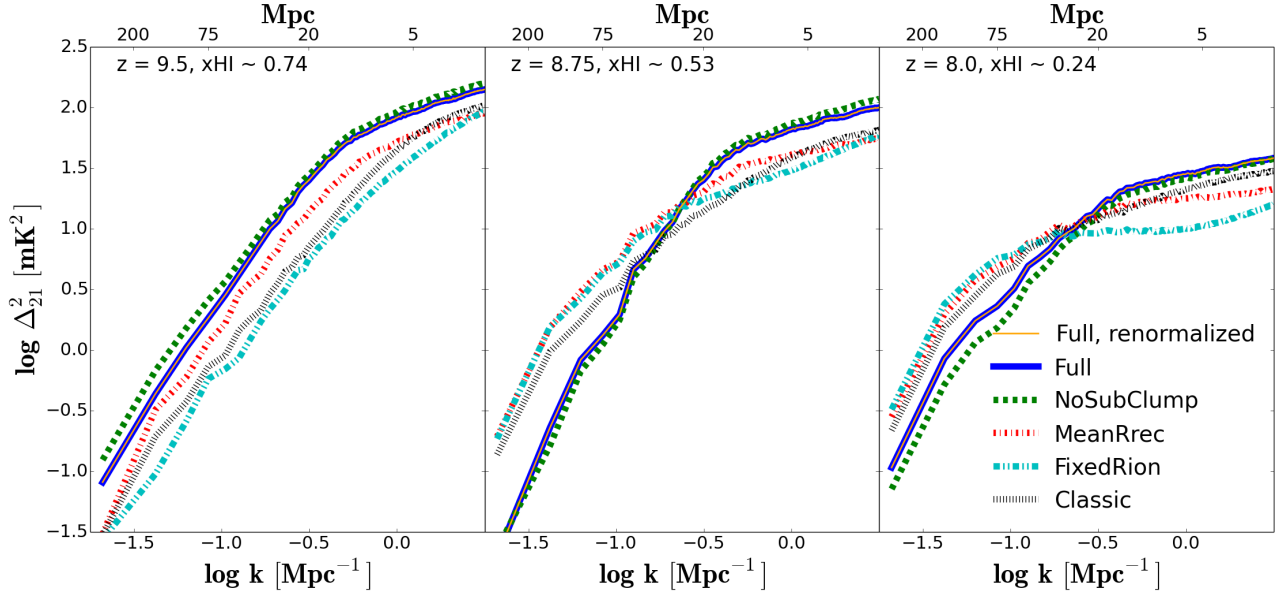


**Figure 13.** The power spectra of the 21-cm signal of the five models at different stages during the EoR. Variations in physical assumptions can result in  $\times 2 - 3$  variations in the 21-cm power spectrum such as:  $R_{\text{rec}}$  suppresses the large-scale power spectrum while  $R_{\text{ion}}$  boosts the small-scale power spectrum.

and 21-cm power spectra of our fiducial model (**Full**) to other models at different phases of the EoR, respectively. We begin by comparing the 21-cm power spectra from our fiducial model (**Full**) using the actual  $R_{\text{ion}}$  (blue, solid), that requires  $f_{\text{esc}} = 4\%$  to match the observations excluding SFR function measurements, with the renormalized  $R_{\text{ion}}$  (orange, solid) that requires  $f_{\text{esc}} = 6\%$  to match the SFR functions measurements. We see, as expected, that the 21-cm power spectra with and without the renormalization to  $R_{\text{ion}}$  are identical, which confirms that the normalization of  $R_{\text{ion}}$  can

be directly compensated by tuning our free parameter  $f_{\text{esc}}$  to higher or lower values as implied by observations.

As with the topology, the **Full** and **NoSubClump** models produce approximately similar power spectra of the ionisation fields and 21-cm signal through all EoR phases. The differences in topology at moderate overdensities are sufficiently rare to not impact the overall power spectrum appreciably. This confirms that the sub-clumping effects have little significance to the EoR 21-cm observables.

To further test the effects of sub-grid clumping, we also



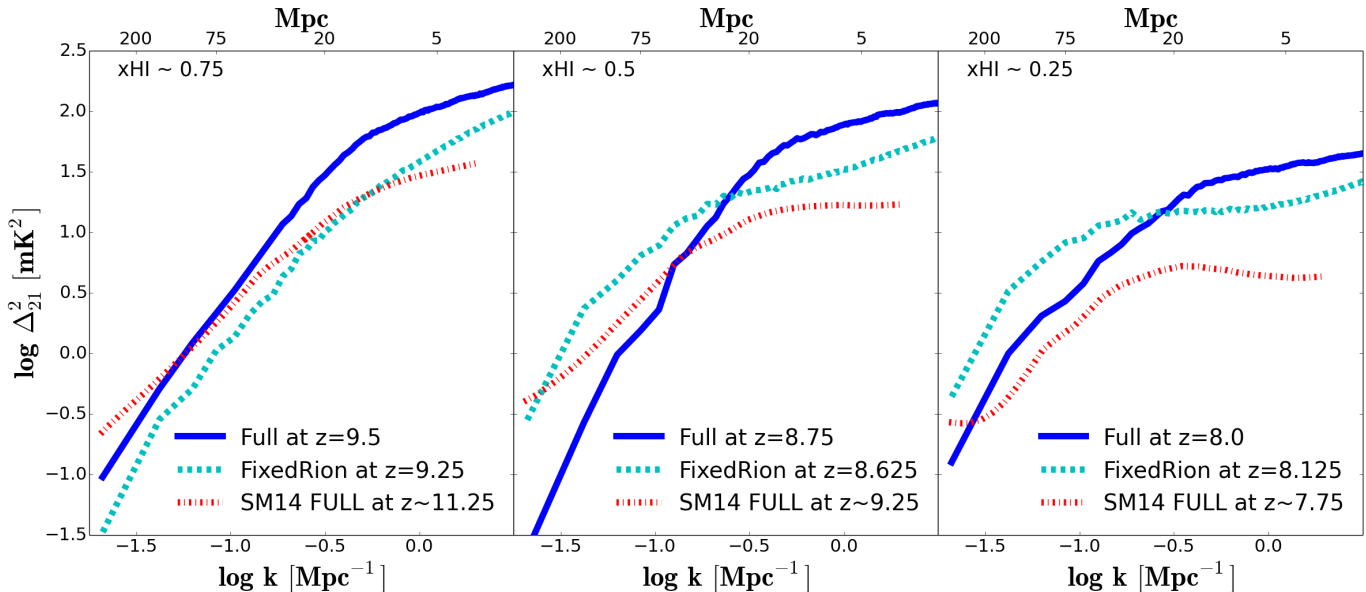


**Figure 14.** Comparison of the predicted 21-cm power spectrum between our **Full** (blue, solid) and **FixedRion** (dashed, cyan) models with the **FULL** model (dash-dotted, red) of SM14 (Sobacchi & Mesinger 2014) at different neutral fraction. It is evident that the shape of the 21-cm power spectrum predicted from **FixedRion** model is similar to that of SM14 **FULL** model at all epochs, since both models share similar physical assumptions. Our **Full** model produces more power on small scales due to introducing non-linearly mass-dependent ionisations via  $R_{\text{ion}}$ .

ran the **NoSubClump** model with the same  $f_{\text{esc}} = 4\%$  that is used in the **Full** model, without matching to the same  $\tau$ . We confirmed that the **NoSubClump** model produces mostly identical results at the same neutral fraction for this slightly different  $f_{\text{esc}}$ . This confirms our finding, that the sub-clumping has no significant contribution to the EoR process, is robust and independent of the way we used to do this comparison with the **Full** model.

As we have seen in studying the overall topology, the **Full** and **NoSubClump** models are very similar, while the **MeanRrec**, **FixedRion**, and **Classic** cases show similar evolutionary trends. Not fully accounting for both non-linear ionisations and inhomogeneous recombinations tends to raise the ionisation field power spectrum on large scales relative to smaller scales, which results in a lower 21-cm power spectrum by a factor of a few. Hence, for instance, compared to the old version of SIMFAST21 during the early stages of the EoR, our new code predicts almost  $4\times$  as much power on large scales, and twice as much on small scales.

The shape of the power spectra continue to be different at later stages, at which time the **Full** model ends up with less large scale power but more small-scale power, as visually evident from the ionisation maps in Figure 9. The physical reasons were discussed in §5.2, but basically arise because properly accounting for recombinations tends to slow the ionisation fronts when compared to **MeanRrec**, while the **FixedRion** produces relatively more photons in low-density regions from low-mass halos which causes more large-scale bubbles. The **MeanRrec**, **FixedRion**, and **Classic** runs themselves show different evolutionary trends, with **FixedRion** increasing its ionisation and 21-cm power spectra faster than the other two.

A comparison of the **MeanRrec** and **Classic** models in Figure 13 illustrates the significance of including a re-

alistic treatment for the dependence of ionising efficiency on halo mass. Both models effectively adopt a spatially-homogeneous recombination rate and are explicitly tuned to reproduce  $\tau$ . However, the **MeanRrec** (like the **Full** model) adopts the ionising efficiency in Figure 1 and Equation (2), which concentrates ionisations in overdense regions. Consequently, the **MeanRrec** model predicts more large-scale power at all times than the **Classic** model. This effect counteracts the suppression of large-scale power owing to spatially-inhomogeneous recombinations (Sobacchi & Mesinger 2014). Note that the adopted dependence in Equation (2) is not arbitrary – it is taken from high-resolution hydrodynamic simulations that have been shown to be consistent with a range of observations of galaxies, absorbers, and reionisation (Finlator et al. 2015). Our results indicate that it is an important factor to consider when predicting the 21-cm power spectrum.

Finally, we compare the predicted 21-cm power spectrum from our new version of SIMFAST21 with those predictions from another semi-numerical simulation (Sobacchi & Mesinger 2014, their **FULL** model) in Figure 14. SM14 **FULL** simulation accounts for inhomogeneous recombinations but uses only homogeneous ionisations via a constant efficiency parameter ( $\zeta$ , similar to our **Classic** model). Thus, the SM14 model shares similar physical assumptions to our **FixedRion** model. From Figure 14, it is clear to see that the shape of the 21-cm power spectrum predicted from **FixedRion** model is qualitatively similar to that of the SM14 model at all epochs, but there is a tendency for the **FixedRion** model to produce somewhat more power as the EoR proceeds; this is possibly related to different density field contribution from different  $z$ . However, it is quite clear that our **Full** model predicts more power on small scales

than models with homogeneous ionisations owing to non-linear ionisations.

To summarize, our new prescription for tracking non-linear ionisations and inhomogeneous recombinations results in predictions that differ significantly from models that do not include these effects, in particular yielding less power on scales of  $\gtrsim 10$  Mpc, but more power on smaller scales. Consistent with Sobacchi & Mesinger (2014), we find that introducing inhomogeneous recombinations suppresses the power spectra of the ionisation field and 21-cm signal on large scales. We also find that introducing non-linear ionisations (via  $R_{\text{ion}}$ ) boosts the small scale power spectra of the ionisation fields and the 21-cm signal. These results highlight the importance of carefully considering the details of ionising sources and recombinations in making accurate predictions for future 21 cm EoR studies.

## 6 CONCLUSION

We have predicted the 21-cm power spectrum during the epoch of reionisation from a new and improved version of our semi-numerical code SIMFAST21. This new version has been modified to incorporate halo mass-dependent ionisation rates ( $R_{\text{ion}}$ ) and density-dependent recombination rates ( $R_{\text{rec}}$ ) rates as a function of redshift. We parameterise  $R_{\text{ion}}$  and  $R_{\text{rec}}$  from small-volume, high-resolution radiative hydrodynamic simulation (**6/256-RT**, Finlator et al. 2015) and a larger cosmological hydrodynamic simulation (**32/512**, Davé et al. 2013), that incorporate galaxy formation physics that has been well-constrained to match a wide range of observations down to lower redshifts. We have implemented these scalings into SIMFAST21 to identify the ionised regions, as opposed to using a uniform ionising efficiency parameter per halo mass ( $\zeta$ ) and no explicit recombinations as in the old version of SIMFAST21. Using this, we have studied the evolution of the neutral fraction and 21-cm power spectrum during reionisation.

Our main key findings are as follows:

- The mass-dependent ionisation rate  $R_{\text{ion}}$  scales super-linearly with halo mass as  $M_h^{1.41}$ , which is consistent with the SFR- $M_h$  relation that previously found by Finlator et al. (2011). The recombination rate  $R_{\text{rec}}$  scale roughly as the density squared, though with deviations at high overdensities. Both display fairly tight relations that can be well-captured by analytic fitting formulae (eq. 2 and eq. 4).

- We tune our one free parameter, the ionising photon escape fraction, to be  $f_{\text{esc}} = 4_{-2}^{+7}\%$ , in order to simultaneously match three key EoR observables: (i) The optical depth to Thomson scattering from Planck (2015); (ii) the ionising emissivity measured at  $z \sim 5$  from Becker & Bolton (2013); (iii) the neutral fraction near end of reionisation from Fan et al (2006); Becker & Bolton et al (2015); McGreer et al. (2015). This low  $f_{\text{esc}}$ , independent of halo mass and redshift, highlights the importance of running large-volume simulations to properly characterise the escape fraction  $f_{\text{esc}}$  and hence the ionising photon budget to complete reionisation. Note that this  $f_{\text{esc}}$  represents the escape fraction averaged over all halos within a  $0.375h^{-1}\text{Mpc}$  (comoving) cells, rather than  $f_{\text{esc}}$  from individual galaxies. To further concurrently match the SFR function measurements by Smit et al. (2012), a renormalization of  $R_{\text{ion}}$  by a factor of 1.5 is required, which

then implies an escape fraction of 6%. This renormalization of  $R_{\text{ion}}$  and  $f_{\text{esc}}$  has no impact on the 21-cm power spectrum or other observables, since the total photon output remains the same.

- During the early EoR, the 21-cm power spectrum drops on large scales while staying constant on small scales, as small ionisation bubbles counteract the overall drop in cosmic HI density. At later stages, the bubbles grow larger and the power on large scales recovers. After the global neutral fraction drops below  $\sim 10\%$  (at  $z \sim 7.5$  in our simulation), the 21-cm power spectrum drops rapidly.

- Reionisation occurs earlier in our SIMFAST21 run than in the 6/256-RT simulation by  $\Delta z \sim 0.5$ , due to the small dynamic range of 6/256-RT that fails to capture the very earliest stages driven by the rarest overdensities, as well as large halos that are important during the later stages of the EoR. These results are well-converged with respect to simulation volume up to scales  $\sim 1/4$  of the box size.

- Introducing non-linearly mass-dependent ionisations ( $R_{\text{ion}}$ ): (i) increases the duration of reionisation; (ii) boosts the 21-cm power at all scales by  $\times 2 - 3$  during the early EoR; (iii) boosts the small-scale 21-cm power by  $\times 2 - 3$  while lowering the large scale ( $\gtrsim 5h^{-1}\text{Mpc}$ ) power during the late EoR. Qualitatively similar trends hold true for the ionisation field power spectra (**Full** versus **FixedRion**).

- Including spatially homogeneous recombinations using a globally-averaged recombination rate results in significantly more power on large scales and less power on small scales, since ionisation bubbles are able to grow to larger scales (**Full** versus **MeanRrec**).

- Including clumping effects on scales below our cell size ( $0.375h^{-1}\text{Mpc}$ ) does not significantly affect the overall EoR topology or 21-cm power spectrum (**Full** versus **NoSubClump**), though it does result in a lower ionisation fraction at moderate overdensities ( $\Delta \sim 5 - 10$ ).

- In agreement with Sobacchi & Mesinger (2014), we find that inhomogeneous recombinations ( $R_{\text{rec}}$ ) matter a great deal (**Full** or **NoSubClump** versus **MeanRrec**) in suppressing the large-scale power spectrum, but accounting further for the detailed dependence of recombination rate on density at scales smaller than our cell size changes results minimally, and only at fairly high overdensities (**Full** versus **NoSubClump**).

- Compared to the previous version of SIMFAST21 (**Classic**), our new version produces more small-scale 21-cm power and less large-scale power. It is generally most similar to a model that assumes a globally-averaged recombination rate (**MeanRrec**) or assumes a constant ionising output per unit halo mass (**FixedRion**).

- The power spectrum from the model of Sobacchi & Mesinger (2014) that account for recombinations but retain a fixed ionising output per unit halo mass is qualitatively similar to our **FixedRion** case, albeit with generally a lower amplitude.

- Our **Full** model shows a significantly higher median halo mass for ionizing photon output of  $\sim 10^{10}M_{\odot}$ , as opposed to  $\sim 10^{8.5}M_{\odot}$  in the case of a constant ionising efficiency. This suggests that the majority of galaxies responsible for reionisation may be detectable with *Webb*; we leave a more detailed examination of this for future work.

- Incorporating the non-linear mass-dependent ionisation causes reionisation to complete at a later epoch by  $\Delta z \sim 1$ ;

this is a larger impact than that obtained by varying the recombination methodology.

Taken together, our results suggest that the details of how one models ionisation and recombinations can impact the strength and shape of the 21-cm power spectrum up to a factor of  $\sim \times 3$ . This is smaller than current observational uncertainties which are dominated by systematics, but might be significant for upcoming facilities such as HERA and SKA-Low. This work represents a step forward in accurately modeling the physical processes occurring during reionisation on large scales. In the future we will use these models to make more detailed predictions for the observability of the 21-cm power spectrum at various observationally-accessible epochs and scales.

We note that we have not considered any potential exotic sources of reionising photons. For instance, a recent paper by Madau & Haardt (2015) argues for quasars contributing significantly more than previously thought, indeed perhaps driving reionisation. Such a population of accreting black holes would provide an additional source of ionising photons that would once again vary how reionisation proceeds. Likewise, our radiation-hydrodynamic simulation did not properly track the contribution of mini-halos (i.e. those below the H cooling limit) to the ionising photon budget during reionisation, but there are no observational constraints that limit this. Our SIMFAST21-based modeling framework provides a way to explore these variations and their impact on observables such as the 21-cm power spectrum, in order to facilitate more optimal scientific interpretation of forthcoming 21-cm and other EoR observations.

## ACKNOWLEDGEMENTS

The authors acknowledge helpful discussions with Andrei Mesinger, Sourav Mitra, Suman Majumdar, Marta Silva and Daniel Cunnama. SH is supported by the Deutscher Akademischer Austauschdienst (DAAD) Foundation. RD and SH are supported by the South African Research Chairs Initiative and the South African National Research Foundation. MGS acknowledges support from the South African Square Kilometre Array Project, the South African National Research Foundation (grant 92788) and FCT under grant PTDC/FIS-AST/2194/2012. This work was also supported by NASA grant NNX12AH86G. Part of this work was conducted at the Aspen Center for Physics, which is supported by National Science Foundation grant PHY-1066293. Computations were performed at the cluster “Baltasar-Sete-Soi”, supported by the DyBHo-256667 ERC Starting Grant, and the University of the Western Cape’s “Pumbaa” cluster.

## REFERENCES

- Barkana, R. & Loeb, A. 2001, *Phys. Rep.*, 349, 125  
 Bauer, A., Springel, V., Vogelsberger, M., Genel, S., Torrey, P., Sijacki, D., Nelson, D., Hernquist, L., 2015, *MNRAS*, 453, 3593.  
 Becker, Robert H.; Fan, Xiaohui. et al 2001, *AJ*, 122, 2850.  
 Becker, G. D., Bolton, J. S. 2013, *MNRAS*, 436, 1023  
 Becker, G. D., Bolton, J. S., Madau, P., Pettini, M., Ryan-Weber, E. V., Venemans, B. P., 2015, *MNRAS*, 447, 3402  
 Behroozi, P. S., Wechsler, R. H., Conroy, C., 2013, *ApJ*, 770, 57.  
 Chabrier G., 2003, *PASP*, 115, 763  
 Choudhury T. R., Haehnelt M. G., Regan J., 2009, *MNRAS*, 394, 960  
 Chardin, J., Haehnelt, M. G., Aubert, D., Puchwein, E. 2015. eprint arXiv:1505.01853.  
 Davé, R., Katz, N., Oppenheimer, B. D., Kollmeier, J. A., Weinberg, D. H. 2013, *MNRAS*, 434, 2645  
 Davé, R., Oppenheimer, B. D., Finlator, K. M. 2011, *MNRAS*, 415, 11  
 Davé, R., Finlator, K. M., Oppenheimer, B. D. 2011, *MNRAS*, 416, 1354  
 Dekel, A. et al. 2009, *Nature*, 457, 451  
 Fan, X., Carilli, C.L., Keating B. 2006, *Annual Review of Astronomy and Astrophysics*, 44, 415  
 Finlator, K. Özel, F. & Davé, R. 2009, *MNRAS*, 393, 1090  
 Finlator, K., Davé, R., Özel, F. 2011, 743, 169  
 Finlator, Kristian; Oh, S. Peng; Davé, R., Özel, F. , 2012, *MNRAS*, 427, 2464.  
 Finlator, Kristian; Muoz, Joseph A.; Oppenheimer, B. D.; Oh, S. Peng; Özel, F. & Davé, 2013, *MNRAS*, 436, 1818  
 Finlator, K., Thompson, R., Huang, S., Davé, R., Zackrisson, E., Oppenheimer, B. D. 2015, *MNRAS*, 447, 2526  
 Villaescusa-Navarro F., Viel M., Datta K. K., Choudhury T. R., 2014, *J. Cosmol. Astropart. Phys.*, 050  
 Furlanetto, S. R., Oh, S. P., & Briggs, F. H. 2006, *PHYS REP*, 433, 181  
 Gabor, J. M. & Davé, R. 2012, *MNRAS*, 427, 1816  
 Gabor, J. M. & Davé, R. 2015, *MNRAS*, 447, 374  
 Gnedin, N. Y. 2000, *ApJ*, 542, 535  
 Gnedin, N. Y.; Kravtsov, A. V.; Chen, H. 2008, *ApJ*, 672, 765.  
 Gnedin, N. Y.; Kaurov, A. A. 2014, *ApJ*, 793, 30  
 Haardt, F., & Madau, P. 2012, *ApJ*, 746, 125  
 Haardt, F. & Madau, P. 2001, in Neumann D. M., Van J. T. T., eds, *Proc. Clusters of galaxies and the high redshift universe observed in X-rays, Recent results of XMM-Newton and Chandra, XXXVth Rencontres de Moriond , XXIst Moriond Astrophysics Meeting*. University of California, Santa Cruz, US.  
 Hinshaw, G. et al. 2013, *ApJS*, 208, 19  
 Hui, L., Gnedin, N. Y., 1997, *MNRAS*, 292, 27  
 Iliev, I. T., Mellema, G., Ahn, K., et al. 2014, *MNRAS*, 439, 725  
 Iliev, Ilian T.; Santos, Mario G.; Mesinger, Andrei; Majumdar, Suman; Mellema, Garrelt; 2015 *Proc. Sci.*, Epoch of Reionization modelling and simulations for SKA. SISSA, Trieste, PoS (AASKA14) 007.  
 Iliev, I. T.; Mellema, G.; Pen, U.-L.; Merz, H.; Shapiro, P. R.; Alvarez, M. A. 2006, *MNRAS*, 369, 1625.  
 Katz, N., Weinberg, D. H., Hernquist, L. 1996, *ApJS*, 105, 19  
 Kaurov, A. A. and Gnedin, N. Y. 2014, *ApJ* 787(2),146.  
 Kaurov, A. A. and Gnedin, N. Y. 2015, arXiv:1412.5607.  
 Kuhlen, M., & Faucher-Giguère, C.-A. 2012, *MNRAS*, 423, 862  
 Kulkarni, G., Rollinde, E., Hennawi, J. F., Vangioni, E., 2013, *ApJ*, 772, 93  
 McGreer, I. D., Mesinger, A., D’Odorico, V., 2015, *MNRAS*, 447, 499.  
 La Plante, P., Battaglia, N., Natarajan, A., Peterson, J.

- B., Trac, H., Cen, R., Loeb, A., 2014, *ApJ*, 789, 31.
- Lidz, A., Zahn, O., McQuinn, M., Zaldarriaga, M., Hernquist, L., 2008, *ApJ*, 680, 962.
- Majumdar S., Mellema G., Datta K. K., Jensen H., Choudhury T. R., Bharadwaj S., Friedrich M. M., 2014, *ArXiv e-prints*, arXiv:1403.0941
- Mesinger A., Furlanetto S., 2007, *ApJ*, 669, 663
- Ma, X., Kasen D., Hopkins P. F., et al 2015, arXiv:1503.07880
- Madau P., Haardt F. 2015, arXiv:1507.07678
- Mitra, S., Choudhury T. R., Ferrara A., 2011, *MNRAS*, 413, 1569.
- Mitra, S., Choudhury T. R., Ferrara A., 2012, *MNRAS*, 419, 1480.
- Mitra, S., Ferrara, A., & Choudhury, T. R. 2013, *MNRAS*, 428, L1
- Mitra, S., Davé, R., Finlator, K. 2015, *MNRAS*, 452, 1184
- Mitra S, Choudhury T. R., Ferrara A. 2015, arXiv:1505.05507
- Mellema, G., Iliiev, I. T., Pen, U.-L., & Shapiro, P. R. 2006, *MNRAS*, 372, 679
- McQuinn, M., Lidz, A., Zahn, O., et al. 2007, *MNRAS*, 377, 1043
- Oppenheimer, B. D. & Davé, R. 2008, *MNRAS*, 387, 577
- Pawlik, A. H.; Schaye, J., 2008, *MNRAS*, 389, 651
- Pentericci, L. et al. 2014, *ApJ*, 793, 113
- Popping, A., Davé, R., Braun, R., Oppenheimer, B. D. 2009, *A&A*, 504, 15
- Raičević, M., Theuns, T., 2011, *MNRAS*, 412, L16.
- Razoumov, A. O., Norman, M. L., Abel, T., & Scott, D. 2002, *ApJ*, 572, 695
- Robertson, Brant E.; Ellis, Richard S.; Furlanetto, Steven R.; Dunlop, James S. 2015, *ApJ*, 802, 19.
- Planck Collaboration XIII, Ade, P. A. R., Aghanim, N., et al. 2015, arXiv:1502.01589 [PC15]
- Santos M. G., Ferramacho L., Silva M. B., Amblard A., Cooray A. 2010, *MNRAS*, 406, 2421
- Smit, R., Bouwens, R. J., Franx, M., Illingworth, G. D., Labb, I., Oesch, P. A.; van Dokkum, P. G., 2012, *ApJ*, 756, 14.
- So, G. C., Norman, M. L.; Reynolds, D. R.; Wise, J. H. 2014, *ApJ*, 789, 149.
- Sobacchi E., Mesinger A., 2014, *MNRAS*, 440, 1662
- Somerville, R. S., Popping, G., Trager, S. C. 2015, eprint arXiv:1503.00755
- Springel, V. & Hernquist, L. 2003, *MNRAS*, 339, 289
- Springel, V. & Hernquist, L. 2003, *MNRAS*, 339, 312
- Springel, V. 2005, *MNRAS*, 364, 1105
- Sutherland, R. S. & Dopita, M. A. 1993, *ApJS*, 88, 253
- Schaerer, D. 2003, *A&A*, 397, 527
- Schauer, A. T. P., Whalen D. J., Glover S. C. O., Klessen R. S., 2015 arXiv:1506.04796.
- Thomas, R. M., Zaroubi, S., Ciardi, B., et al. 2009, *MNRAS*, 393, 32
- Tilvi, V., et al, 2013. *ApJ*, 768, 56.
- Verner, D. A. & Ferland, G. J. 1996, *ApJS*, 103, 467
- Wise, J. H., & Cen, R. 2009, *ApJ*, 693, 984
- Wise, J. H., Demchenko, V. G., Halicek, M. T., et al. 2014, *MNRAS*, 442, 2560
- Zel'Dovich Y. B., 1970, *A&A*, 5, 84
- Zahn O., Lidz A., McQuinn M., Dutta S., Hernquist L., Zaldarriaga M., Furlanetto S. R., 2007, *ApJ*, 654, 12
- Zahn O., Mesinger A., McQuinn M., Trac H., Cen R., Hernquist L. E., 2011, *MNRAS*, 414, 727